

# Unified Few-shot Crack Segmentation and its Precise 3D Automatic Measurement in Concrete Structures

Pengru Deng<sup>1,2</sup> | Jiapeng Yao<sup>1</sup> | Chun Li<sup>3</sup> | Su Wang<sup>4</sup> | Xinrun Li\*<sup>5</sup> | Varun Ojha<sup>5</sup> |  
Xuhui He<sup>1,2</sup> | Takashi Matsumoto<sup>6</sup>

<sup>1</sup>School of Civil Engineering, Central South University, Changsha, China

<sup>2</sup>Hunan Provincial Key Laboratory for Disaster Prevention and Mitigation of Rail Transit Engineering Structures, Changsha, China

<sup>3</sup>Carizon, Shanghai, China

<sup>4</sup>Nvidia, Shanghai, China

<sup>5</sup>School of Computing, Newcastle University, Tyne and Wear, United Kingdom

<sup>6</sup>Faculty of Engineering, Hokkaido University, Sapporo, Japan

## Correspondence

Xinrun Li, School of Computing, Newcastle University, Tyne and Wear, NE4 5TG, United Kingdom

Email: X.Li169@ncl.ac.uk

## Abstract

Artificial Intelligence (AI) has become increasingly essential in concrete crack inspection. However, existing methods often lack adaptability to diverse scenarios, exhibit limited robustness in image-based approaches, and struggle with curved or complex geometries. To address these limitations, an innovative framework for two-dimensional (2D) crack detection, three-dimensional (3D) reconstruction, and 3D automatic crack measurement was proposed by integrating computer vision technologies and multi-modal Simultaneous localization and mapping (SLAM) in this study. Firstly, building on a base DeepLabv3+ segmentation model, and incorporating specific refinements utilizing foundation model Segment Anything Model (SAM), we developed a crack segmentation method with strong generalization across unfamiliar scenarios, enabling the generation of precise 2D crack masks. To enhance the accuracy and robustness of 3D reconstruction, Light Detection and Ranging (LiDAR) point clouds were utilized together with image data and segmentation masks. By leveraging both image- and LiDAR-SLAM, we developed a multi-frame and multi-modal fusion framework that produces dense, colorized point clouds, effectively capturing crack semantics at a 3D real-world scale. Furthermore, the crack geometric attributions were measured automatically and directly within 3D dense point cloud space, surpassing the limitations of conventional 2D image-based measurements. This advancement makes the method suitable for structural components with curved and complex 3D geometries. Experimental results across various concrete structures highlight the significant improvements and unique advantages of the proposed method, demonstrating its effectiveness, accuracy, and robustness in real-world applications.

## KEYWORDS

Automated crack inspection, Crack segmentation, Foundation model refine, 3D reconstruction

## 1 | INTRODUCTION

As the operational lifespan of engineering infrastructures such as bridges and tunnels extends, the issue of structural aging has become increasingly evident and severe largely due to the cumulative effects of loads and environmental factors, leading to significant safety concerns (Hao et al. 2023, Deng et al. 2023b). Concrete structures, renowned for their characteristics such as material availability, cost-effectiveness, and exceptional durability, form the foundation of global infrastructure. Their prevalence is especially evident in China constituting over 80% of all infrastructure (Lu et al. 2024). To ensure the longevity and safety of concrete structures, regular inspections are essential for monitoring the progression of structural properties, which in turn allows for a comprehensive assessment of their health (Liu et al. 2021a). Concrete cracks, which often originate and are observed on structural surface, are key indicators of the

structure's stress state, safety, and durability. Therefore, they are considered essential metrics for assessing structural health and play a pivotal role in inspections (Yang et al. 2018b).

Nevertheless, manual crack inspection, as traditionally performed, suffers from inaccuracies, incompleteness, and significant subjectivity (Kim and Cho 2019). These limitations, along with the challenges of inspecting elevated structures, have driven the development of advanced technologies. As a result, computer vision-based crack detection methods have emerged as a preferred alternative to traditional approaches. However, a key challenge remains: how to develop robust, precise, automated, and standardized solutions for crack inspection (Sun et al. 2020, Yao et al. 2014). Concrete cracks are characterized by their variability in attributes, such as patterns, widths, and lengths. Mechanically, the width and number of cracks are critical markers for assessing the structural integrity and predicting changes in permeability as the structure deteriorates (Feng et al. 2023). The spatial distribution and orientation of cracks provide

insights into their types, whether they are structural or non-structural, and their underlying causes (Zeng et al. 2024). Given the inherent spatial attributes of cracks, 3D perception and measurement are indispensable in computer vision-based crack inspection. In addition, practical applications may face certain challenges. Firstly, due to variables such as complex textures, varying lighting conditions, and stains or spots, it is difficult to distinguish cracks from the intricate background present in concrete structures. Particularly, the subtle appearance of small and narrow cracks can be easily concealed by background noise. Secondly, the quality of images used for analysis varies significantly due to factors such as resolution, focus, and capture angle. As a result, developing method that is robust and can effectively generalized across diverse scenarios and structures with high accuracy is critically important and challenging.

Therefore, it is evident that three key requirements must be met to achieve automated, comprehensive and practically meaningful concrete crack inspection: first, efficient capture of 3D spatial characteristics, including dimensions, distributions, and orientations; second, high-precision detection given the submillimeter dimensions of real cracks (Ding et al. 2023, Deng et al. 2023a); and third, minimal dependence on specific datasets, enabling generalization across various scenarios.

In order to address the above-mentioned concerns in the concrete crack inspection based on computer vision, our work proposes an accurate and robust pipeline for crack detection and reconstruction by using computer vision foundation models and SLAM. To boost the accuracy and quality of 3D crack reconstruction, a high-precision dense scene reconstruction is achieved by integrating LiDAR and Inertial Measurement Unit (IMU) data using a tightly coupled SLAM algorithm. The reconstruction process is further optimized through a crack reconstruction module that employs the Moving Least Squares (MLS) algorithm and multi-frame pixel fusion, leveraging photometric and multi-view consistency. Additionally, the Segment Anything Model (SAM) (Kirillov et al. 2023), a versatile 3D segmentation foundation model, is combined with segmentation models trained with few-shot samples to reduce the dataset requirements. Within this framework, SAM operates as a refiner, focusing results enhancements within carefully defined Regions of Interest (ROIs). Ultimately, an automatic and high-quality 3D crack reconstruction and quantification is achieved by integrating semantic data from cameras with dense LiDAR reconstructions using a multimodal fusion algorithm. This advancement facilitates precise spatial analysis and supports the execution of related downstream tasks. The novelty and contributions of this paper can be summarized as follows:

1. A handheld 3D crack inspection system was developed, integrating hardware design and multi-sensor calibration.
2. A few-shot concrete crack segmentation method based on foundation model, SAM was introduced, enabling effective generalization to diverse crack scenarios.
3. A multi-frame and multi-modal fusion framework allowed accurate 3D reconstruction, generating a dense point cloud with crack semantics and real-world scaling.
4. An automated 3D crack measurement system adaptable to various structural geometries.

The remainder of this paper is organized as follows:

Section 2 discusses related studies, and Section 3 to Section 7 explain the system architecture and methodology in detail. In Section 8 and 9, the on-field experiments and performance are evaluated. Finally, Section 10 presents the conclusions.

## 2 | LITERATURE REVIEW

### 2.1 | Challenges of Generalization in Concrete Surface Defect Perception

Inspired by the success of deep learning algorithms in medical computer vision, Zhang et al. (2016) pioneered the application of convolution neural networks (CNN) for crack classification in asphalt pavements. Since then, numerous scholars have explored the field of crack image recognition, focusing primarily on three key areas: crack image classification, crack region detection, and pixel-level segmentation. Early research in crack classification and detection (Cha et al. 2017, Silva and Lucena 2018, Tang et al. 2022, Chaiyasarn et al. 2018) was primarily concerned with identifying general crack regions, without the ability to delineate precise boundaries or shapes, thereby necessitating the development of more advanced pixel-level segmentation techniques. For pixel-level segmentation, Yang et al. (2018b) employed Fully Convolutional Networks (FCNs) to automate the segmentation of crack images, marking a significant step forward in the automation of the process. Subsequent developments, such as the work by Flah et al. (2020), built upon crack segmentation by incorporating regional image detection to quantify the size and orientation of cracks, thereby advancing the field toward quantitative crack analysis. These advancements have not only led to models that can match or even surpass human accuracy in identifying cracks but have also highlighted the importance of precision in crack segmentation tasks (Zhou et al. 2022 2023, Sun et al. 2024, Chu and Chun 2024, Chun and Kikuta 2024, Huang et al. 2024, Pantoja-Rosero et al. 2022). However, the performance of these models is typically evaluated on the same dataset. Their performance efficacy can be significantly diminished when applied to new scenarios. That is, while these models show high precision within their trained datasets, they often face challenges when generalized to new contexts.

To cater to diverse applications, a variety of open-source crack datasets have been created, covering different structural surfaces and scenarios such as concrete structures, asphalt pavements, and ceramic tiles, as documented by various researchers including (Dais et al. 2021, Ahmadi et al. 2018, Junior et al. 2021, Pak and Kim 2021, Zou et al. 2012, Liu et al. 2019). Each study has generated specialized datasets for specific scenarios within their areas of focus. Indeed, in practical engineering, each instance of crack detection is essentially a new segmentation scenario. Despite the existence of various datasets, there is still a considerable data bottleneck when compared to the standards set by state-of-the-art semantic segmentation tasks. The effectiveness of models in new environments is often constrained by the quality and volume of available training data, a challenge insufficiently addressed in existing research. Relying on extensive, high-resolution datasets for generalization across diverse scenarios is impractical due to the substantial time and labor required. While Domain Adaptation (DA) Liu et al. (2021b) and unsupervised domain adaptation

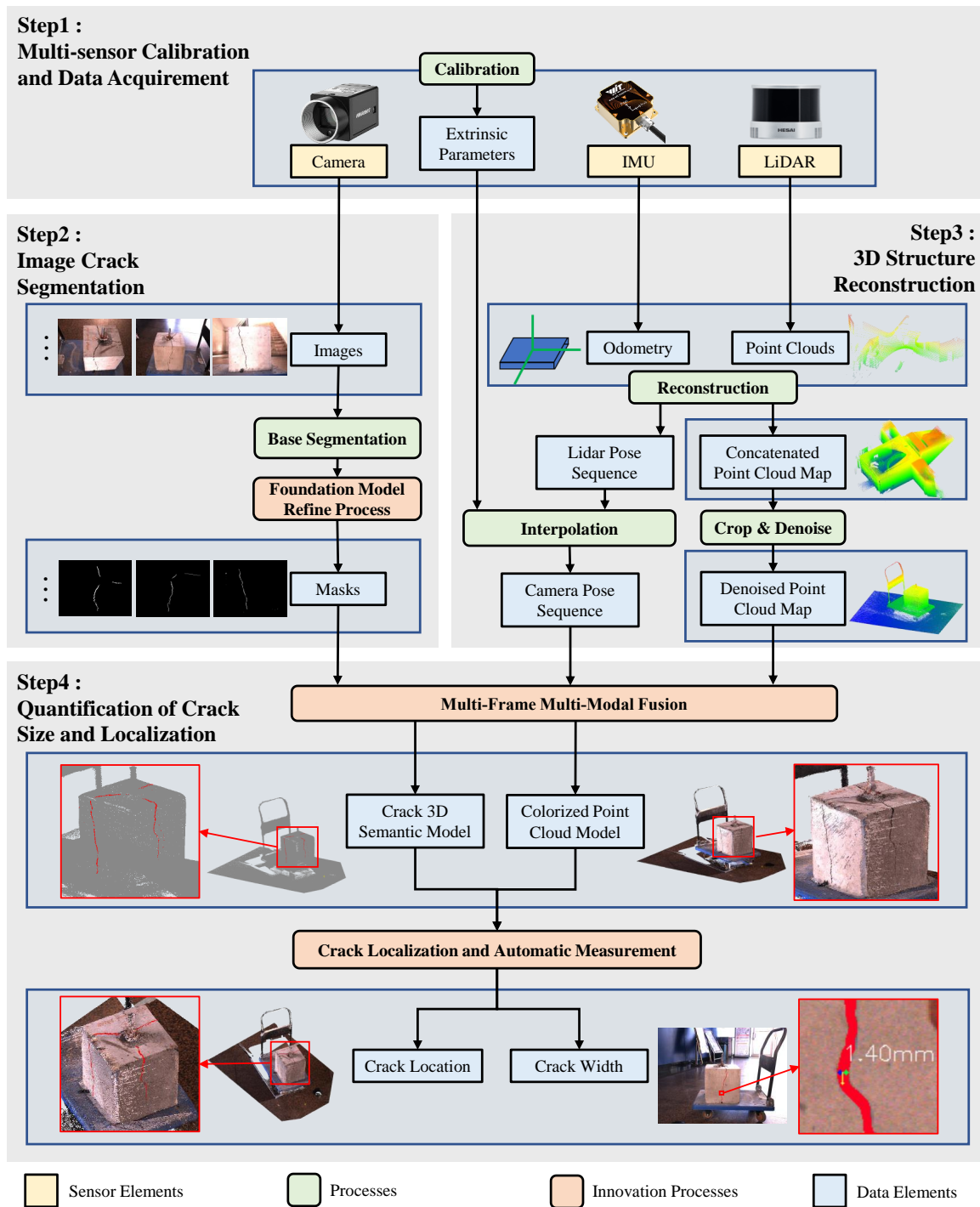


**FIGURE 1** The proposed framework’s workflow involves several steps. First, the camera, LiDAR, and IMU are associated through extrinsic calibration. The LiDAR generates point clouds for LIO and 3D reconstruction. Concurrently, the camera provides images for semantic segmentation. Using a fusion module and post-processing, automatic crack detection and reconstruction are achieved.

(UDA) Zou et al. (2018) have been investigated these approaches often suffer from complexity and insufficient robustness, making them ineffective for real-world applications. This work addresses these limitations by utilizing recent advancements in foundation models in computer vision, providing scalable and efficient solutions for improved model adaptability.

## 2.2 | Generalization Enhancement with Foundation Models

In recent years, an increasing number of foundation models have been introduced, such as Generative Pre-trained Transformer 4 (GPT-4) (OpenAI et al. 2024), SAM (Kirillov et al. 2023), Contrastive Language–Image Pre-training (CLIP) (Radford et al. 2021), Emerging Properties in Self-Supervised Vision Transformers (DINO) (Caron et al. 2021) and others. These models are designed to enhance generalization in deep learning and to be adaptable across a wide range of tasks. For instance, large language models (LLMs) like LLaMA (Touvron et al. 2023) and GPT (OpenAI et al. 2024) have demonstrated exceptional performance in natural language processing. Furthermore, vision-language models (VLMs) like LLaVa (Liu et al. 2023) have successfully merged visual and textual data, laying the groundwork for more holistic and adaptable AI applications.

In the field of computer vision, foundation models have recently emerged as a transformative force. These models, such as CLIP and SAM, demonstrate exceptional zero-shot capabilities and high generalization across diverse tasks. This is largely attributed to their extensive pre-training on large datasets, which enables them to adapt to new vision concepts through innovative prompt-based task designs. A case in point is SAM, introduced by Kirillov et al. (2023). This model was trained on the vast SA-1B dataset, which includes over 11 million images and 1.1 billion masks. SAM leverages various prompts, ranging from bounding boxes and points to masks, to perform segmentation tasks across a spectrum of scenarios. It has achieved state-of-the-art performance in zero-shot settings on numerous datasets. The evolution of SAM has led to enhanced models such as SAM-HQ (Ke et al. 2024), which further refine feature through global-local fusion designs. Additionally, RAP-SAM (Xu et al. 2024) extends the capability to perform real-time processing and is equipped with a streamlined encoder and a unified decoder.

While vision foundation models have advanced considerably, their potential in concrete crack inspection has yet to be fully realized. A major challenge lies in the nature of cracks, which often emerge at the peripheries of local semantic clusters and differ significantly from typical semantic patterns. Consequently, without the integration of prior knowledge, the performance of these models is prone to instability. Rather than developing entirely new foundation models, we introduce an innovative method that harnesses both conventional techniques and foundation models to address these challenges. Specifically, we transform imperfect crack segmentation outputs into prompts, which are subsequently refined at the pixel level through the foundation model SAM. Experimental results indicate that this strategy significantly enhances the performance and adaptability of segmenting cracks on concrete surfaces.

## 2.3 | Crack 3D Reconstruction and Measurement

As mentioned above, accurately determining the 3D spatial features of cracks, such as their dimensions, distribution, and orientation, is essential to evaluate structural damage. Several researchers have utilized single-frame image data to reconstruct crack skeletons and measure crack width (Shokri et al. 2022,

Zhang et al. 2023). However, relying exclusively on a single frame and its associated processing techniques is insufficient for capturing the complete 3D details of cracks. To address this limitation and generate comprehensive 3D crack information, researchers have expanded detection from individual frames to entire structures using reconstruction techniques (Yang et al. 2018a, Mirzazade et al. 2023, Feng et al. 2023, Deng et al. 2023a, Zeng et al. 2024). These reconstruction methods are typically categorized into two categories: SfM-based and SLAM-based approaches.

Significant research has focused on enhancing SfM-based methods for crack localization and measurement in engineering structures. For example, Kim et al. (2022) used a dual-lens system combining wide-angle and telephoto lenses to improve crack detection accuracy. Similarly, Ding et al. (2023) deployed drones equipped with cameras and laser rangefinders for 3D reconstruction and crack measurement. In another study, Zhao et al. (2024) employed UAV photogrammetry for generating 3D reconstructions of dams and extracting crack data. Zeng et al. (2024) demonstrated a practical approach using mobile phones for beam imaging, coupled with open-source software like COLMAP and OpenMVS for 3D crack reconstruction. However, despite the advancements, SfM-based methods still face significant limitations when applied to real-world engineering structures, particularly in terms of structural geometry, reconstruction quality, and scene complexity. For instance, crack width measurements often rely on the assumption of a planar surface, which limits their applicability to complex or irregular geometries. Furthermore, feature-point-based reconstruction methods require substantial image overlap and precise trajectory planning, posing challenges in dynamic or large-scale environments. These methods also struggle with real-time processing due to computational demands.

The second category includes SLAM-based methods, which enable advanced 3D reconstruction through real-time pose estimation and mapping. Yang et al. (2023) used the ORB-SLAM2 framework to reconstruct 3D structures with embedded crack information, employing RGB-D cameras for visual localization. Deng et al. (2023a) introduced a Visual SLAM (VSLAM) method for determining the 3D position and length of cracks, though crack width was not addressed. These vision-based SLAM methods generate point clouds from visual data, which are refined through bundle adjustment (BA), with cracks visualized as colored point clouds. However, these reconstructions are highly sensitive to lighting conditions, which can interfere with feature detection and matching, thereby compromising stability. Variations in lighting may introduce optimization errors, reducing measurement accuracy. Furthermore, while bundle adjustment improves the point cloud, it can also introduce artifacts, such as compression or collapse, which degrade precision. In large-scale environments with insufficient constraints, cumulative errors during bundle adjustment can lead to drift.

Recent advancements in autonomous driving have spurred progress in multi-sensor fusion SLAM techniques (Zhang and Singh 2014, Du et al. 2020, Xu and Zhang 2021, Lin and Zhang 2022, Xu et al. 2022). By combining LiDAR and RGB cameras, these systems enable efficient 3D reconstruction of engineering structures and generate high-quality point clouds for crack semantic segmentation. In crack detection, Hu et al. (2024) demonstrated local crack width measurement using single-frame multi-modal fusion, overcoming the SfM plane assumption's limitations. Similarly, Feng et al. (2023) used multi-frame and multi-modal fusion for crack localization and quantified crack width

through pixel measurements in 2D images. Current reconstruction algorithms, such as R3LIVE (Lin and Zhang 2022), rely on two main components: LiDAR-Inertial Odometry (LIO) and Visual-Inertial Odometry (VIO). However, the VIO reconstruction part requires the camera to have a very high frame rate. At similar cost, this severely limits the image resolution, making it difficult to meet the requirements of high-precision crack image segmentation and reconstruction at the millimeter level, which limits its practical engineering applicability. Moreover, existing methods typically separate crack width measurement from crack localization—measuring the width on 2D images and localizing cracks in 3D point clouds, which results in a lack of synchronized quantification. This separation hinders the simultaneous and automated quantification of both the position and width of the crack. Solving this issue is crucial for periodic inspections and damage assessments of engineering structures and is a key enabler for digital twin technology in structural monitoring.

### 3 | SYSTEM ARCHITECTURE

This work proposes a framework for automated crack detection in engineering structures. The framework innovatively integrates SLAM and computer vision technologies for crack detection, achieving crack localization and automatic quantification of crack width through 3D reconstruction of structures with cracks, as shown in Figure 1. The framework consists of four main components: Multi-sensor Calibration and Data Acquisition; Image Crack Segmentation; 3D Structure Reconstruction and Quantification of Crack Size and Localization. Furthermore, tests were conducted on concrete cubic specimens and concrete slabs with pre-existing cracks to validate the feasibility and accuracy of the proposed framework.

### 4 | MULTI-SENSOR CALIBRATION

Accurate extrinsic calibration is essential for precise data fusion among LiDAR, camera, and IMU sensors. For both camera-IMU and camera-LiDAR extrinsic calibration, the goal is to determine the relative rotation and translation between the sensors to align their coordinate frames.

In the case of camera-IMU calibration, the Kalibr toolbox (Furgale et al. 2012 2013) is commonly used, applying full-batch optimization. This method uses splines to model the system’s pose over time and estimates both the rotation and translation between the camera and IMU.

As shown in Figure 2, a 3D point in the LiDAR coordinate system, represented as  $\mathbf{P}_L = [X_L \ Y_L \ Z_L]^T$ , can be transformed to the camera coordinate system  $\mathbf{P}_C = [X_C \ Y_C \ Z_C]^T$  using the corresponding rotation and translation parameters:

$$\mathbf{P}_C = \mathbf{R}_L^C \mathbf{P}_L + \mathbf{t}_L^C. \quad (1)$$

For camera-LiDAR calibration, the task is to determine the relative rotation matrix  $\mathbf{R}_L^C \in SO(3)$ , where  $SO(3)$  denotes the special orthogonal group in three dimensions. This group represents the set of rotation matrices that preserve vector lengths and orientations. Additionally, the translation vector  $\mathbf{t}_L^C$  is required. Together, these two quantities define the transformation from

the LiDAR frame to the camera frame, which is essential for aligning the two sensors.

Next, to project the transformed 3D point onto the camera’s image plane, we utilize the camera’s intrinsic matrix  $\mathbf{K}$ . Specifically:

$$\mathbf{K} = \begin{bmatrix} f_x & 0 & c_x \\ 0 & f_y & c_y \\ 0 & 0 & 1 \end{bmatrix}, \quad (2)$$

where  $f_x$  and  $f_y$  are the focal lengths of the camera in the  $x$ - and  $y$ -directions, respectively, and  $c_x$  and  $c_y$  are the coordinates of the principal point, typically located at the center of the image. These parameters are obtained through camera calibration. The intrinsic matrix is crucial for converting the 3D point coordinates in the camera frame to 2D pixel coordinates on the image plane. The projection is performed using the following equation:

$$\mathbf{P}_C^{uv} = \mathbf{K} \begin{bmatrix} X_C/Z_C & Y_C/Z_C & 1 \end{bmatrix}^T, \quad (3)$$

where  $\mathbf{P}_C^{uv} = [u, v]^T$  represents the 2D image coordinates of the point in the camera’s image plane.

To project a 3D point from the LiDAR frame to the image plane, the transformation from the LiDAR frame to the camera frame is first applied using the rotation matrix  $\mathbf{R}_L^C$  and the translation vector  $\mathbf{t}_L^C$ . After transforming the point to the camera frame, we use the intrinsic matrix  $\mathbf{K}$  to project the point onto the image plane. The resulting projection is given by:

$$\mathbf{P}_L^{uv} = \mathbf{K} \left[ \left( \mathbf{R}_L^C \mathbf{P}_L + \mathbf{t}_L^C \right) / Z_C \right], \quad (4)$$

where  $\mathbf{P}_L^{uv} = [u, v]^T$  are the 2D image coordinates corresponding to the LiDAR point  $\mathbf{P}_L$  after the transformation and projection.

To enhance the robustness and usability of the calibration process, the existing Direct LiDAR-Camera (DVL) calibration method (Koide et al. 2023) was employed. This method, inspired by end-to-end keypoint detection and Graph Matching Networks (Li et al. 2019), follows a three-step pipeline: preprocessing, initial estimation, and refinement. During the data preprocessing stage, a dense point cloud model is initially generated from motion, capturing detailed scene geometry to facilitate the subsequent minimization of image-point cloud matching errors. In the initial estimation step, the DVL work uses SuperGlue pipeline (Sarlin et al. 2020) to find correspondences between LiDAR intensity images and camera images. It first detects keypoints on camera images and LiDAR intensity images and then finds correspondences between the keypoints using Attentional Graph Neural Network. This approach, which replaces handcrafted heuristics with a powerful neural model in the learnable middle-end, marks a significant milestone toward the realization of end-to-end deep SLAM.

This initial step provides a preliminary estimate of the transformation parameters; however, it remains susceptible to errors caused by noise and outliers in the data. To enhance the accuracy of the extrinsic, the DVL work employs the normalized information distance (NID) (Stewart and Newman 2012) during the refinement phase. The NID is computed by transforming the LiDAR points  ${}^L p_j \in \mathcal{P}_i$  into the camera frame and projecting them into the image space  $x_j = \pi({}^C T_L {}^L p_j)$ . Using the LiDAR point intensities  $\mathcal{L}_j$  and the corresponding pixel intensities  $\mathcal{I}_i(x_j)$ , we construct the marginal histograms  $P(\mathcal{L}_i)$  and  $P(\mathcal{I}_i)$ , as well as the joint histogram  $P(\mathcal{L}_i, \mathcal{I}_i)$ . From

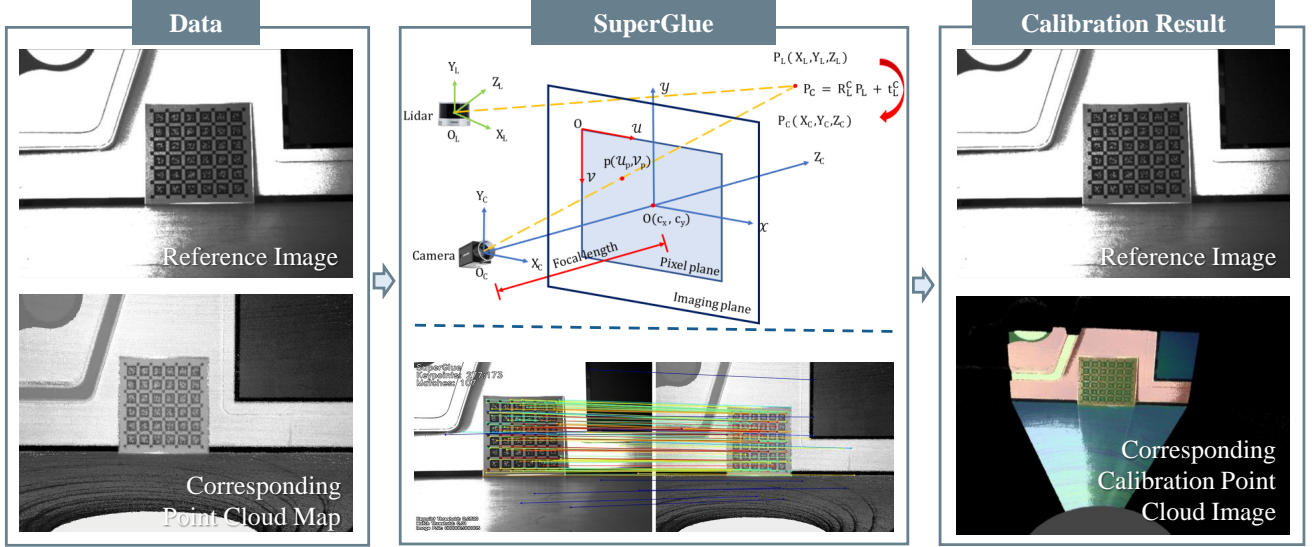


**FIGURE 2** Calibration Process: First, point cloud and image data are collected. Next, the SuperGlue algorithm is used to identify matching points between the point cloud and the image. Using these correspondences, the external transformation matrix is estimated to fuse the point cloud map with the image data. This step involves calculating the relative rotation matrix  $\mathbf{R}_L^C \in SO(3)$  and the translation vector  $\mathbf{t}_L^C$ .

these histograms, we calculate the entropies  $H(\mathcal{L}_i)$ ,  $H(\mathcal{I}_i)$ , and  $H(\mathcal{L}_i, \mathcal{I}_i)$  as follows:

$$H(X) = - \sum_{x \in X} p(x) \log p(x), \quad (5)$$

where  $x$  is each bin in the histogram,  $X$  refers to all bins in the histogram. The NID between  $\mathcal{L}_i$  and  $\mathcal{I}_i$  is then defined as follows:

$$\text{NID}(\mathcal{L}_i, \mathcal{I}_i) = \frac{H(\mathcal{L}_i, \mathcal{I}_i) - \text{MI}(\mathcal{L}_i; \mathcal{I}_i)}{H(\mathcal{L}_i, \mathcal{I}_i)}, \quad (6)$$

$$\text{MI}(\mathcal{L}_i; \mathcal{I}_i) = H(\mathcal{L}_i) + H(\mathcal{I}_i) - H(\mathcal{L}_i, \mathcal{I}_i), \quad (7)$$

$\text{MI}(\mathcal{L}_i; \mathcal{I}_i)$  in Eq. 7 is the mutual information between  $(\mathcal{L}_i)$  and  $(\mathcal{I}_i)$ . The extrinsic parameters can be estimated by minimizing Eq. 6 using the Nelder-Mead optimizer (Nelder and Mead 1965). The NID metric provides a more accurate alignment by considering the statistical dependence between the LiDAR and camera data, leading to a more precise calibration.

## 5 | IMAGE CRACK SEGMENTATION

Traditional 2D crack segmentation methods typically rely on training and testing within fixed datasets. However, their performance often degrades when transferred to new scenarios, necessitating additional annotations. To address this issue, prior works have taken two main approaches.

The first approach formulates the problem as a domain gap between datasets, resolved using supervised domain adaptation (SDA) or unsupervised domain adaptation (UDA). However, such pipelines are often highly complex and yield limited performance improvements. The second approach frames the problem as few-shot learning, aiming to learn semantic features from a small number of annotated samples and apply them to query sets. Yet, this methods

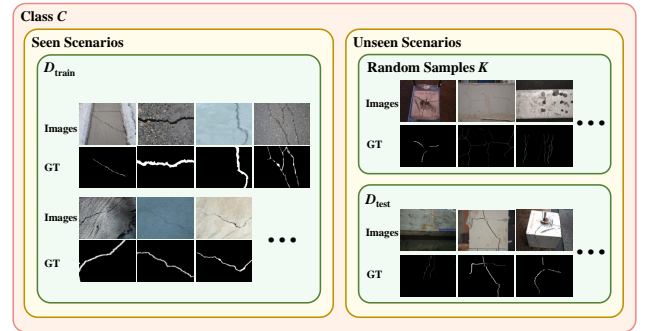


**FIGURE 3** Dataset composition and relationships in K-shot supervised segmentation.

heavily depends on the support set and suffers from limited generalization capabilities. In contrast to these existing methods, our proposed approach leverages the knowledge transfer capabilities of foundation models. Specifically, a domain-specific crack segmentation prompt is designed and tailored to this task.

### 5.1 | Problem Formulation

The 2D segmentation pipeline aim to get accurate crack segmentation mask over images on unseen scenarios, based on the previous work (Wang et al. 2019), this process can be adopted as the following few-shot training and testing protocols.

As shown in Figure 3, supposing that a set of images pertaining to a single class  $C$  is provided, the scenarios are categorized into seen and unseen, with each category containing ground truth annotations (GT). The training set  $D_{\text{train}}$  includes images from the seen scenarios, and the test set  $D_{\text{test}}$  includes images



from the unseen scenarios. The segmentation model  $M$  is trained on  $D_{\text{train}}$  and evaluated on  $D_{\text{test}}$  ( $D_{\text{test}} \cap D_{\text{train}} = \emptyset$ ).

During the test phase for  $K$ -shot supervised segmentation,  $K$  samples are randomly drawn from the unseen scenarios. These samples include  $K$  (image, mask) pairs, representing  $K$  different variations or instances of class  $C$ . The model first extracts knowledge from these samples and then applies this knowledge to perform segmentation on the rest of the data in  $D_{\text{test}}$ . After training, the segmentation model  $M$  is evaluated for its  $K$ -shot segmentation performance on the test set  $D_{\text{test}}$ .

For our experiments, we pre-trained the model using publicly available datasets and evaluated it under 0-shot, 10-shot, and 110-shot settings.

## 5.2 | Base Segmentation Model

In this study, existing segmentation networks, such as DeepLabv3+ (Chen et al. 2018, Zhou et al. 2023), are employed as the base model for crack segmentation due to their established effectiveness in deep learning-based segmentation tasks.

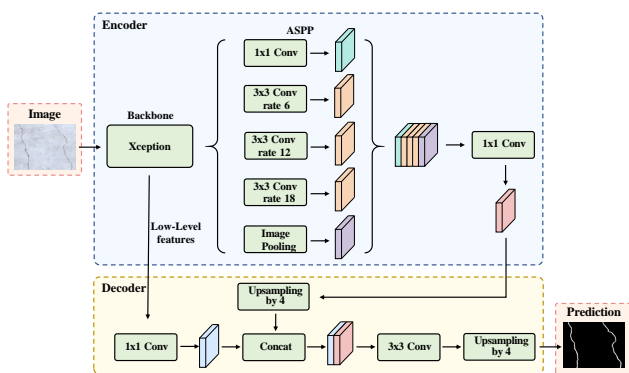


**FIGURE 4** Network structure of DeepLabv3+, where Conv is the convolution layer. The encoder module encodes multi-scale contextual information by applying atrous convolution at multiple scales, while the simple yet effective decoder module refines the segmentation results along object boundaries.

DeepLabv3+ is a state-of-the-art semantic segmentation model that integrates Atrous Spatial Pyramid Pooling (ASPP) with an encoder-decoder architecture to achieve high-precision segmentation, particularly for complex object boundaries. The architecture consists of two main components: the encoder and the decoder, as shown in Figure 4.

The encoder utilizes the Xception network as the backbone, which applies depthwise separable convolutions to reduce computational complexity while maintaining high representational power. Hierarchical feature maps are extracted from the input image, capturing both low-level and high-level features. These maps are then processed by the ASPP module, which employs dilated convolutions with varying dilation rates to capture multi-scale contextual information. By introducing gaps between kernel elements, dilated convolutions expand the receptive field without increasing kernel size, thus preserving spatial resolution. For a given kernel size  $N$  and dilation rate  $d$ , the receptive field of the dilated convolution is equivalent to that of a standard convolution with

kernel size  $(N - 1) \times d + 1$ . This approach mitigates the loss of target feature information typically caused by pooling and downsampling operations in traditional semantic segmentation networks, thus enhancing the model’s ability to capture broader contextual features.

The decoder module refines the segmentation by restoring spatial resolution. The feature maps produced by the encoder are upsampled and integrated with lower-level features to recover fine details that may be lost during the downsampling process. This fusion of high- and low-level features is essential for recovering accurate boundaries, particularly for complex objects. Bilateral upsampling is applied to restore boundary accuracy efficiently, ensuring high-quality segmentation and precise delineation of object boundaries.

## 5.3 | Foundation Model Refine Process

Even though previous crack segmentation methods have shown effectiveness in controlled scenarios, they often struggle under unseen conditions and varying environmental factors. This challenge, known as domain shift, arises from changes in camera intrinsic parameters, hardware properties, and environmental factors such as semantic context and illumination. Recent foundation models built on large-scale datasets like SAM (Kirillov et al. 2023) have shown zero-shot performance across different segmentation tasks. However, when tested on concrete cracks, they struggle to achieve the expected results because cracks often conflict with salient objects in the scene and typically appear at the edges of these objects.

A 2D crack segmentation refinement pipeline, shown in Figure 5, is proposed to address domain shift issues. The pipeline refines segmentation masks by converting imperfect outputs from the base model into point prompts, which are then processed by foundation models. A quality assessment module ensures the reliability of the refined masks. The process includes two core components: prompt generation and quality assessment, as outlined in Sections 5.3.1 and 5.3.2.

### 5.3.1 | Prompt Generation

Observing suboptimal results in the base segmentation model, we noted that the generated masks, while maintaining high accuracy (95%), were incomplete and sparse. A detailed analysis revealed that the main issue lies in low recall, necessitating the enhancement of mask completeness using the base model’s output.

To address this, we utilized the skeleton of the base mask, derived using an Euclidean distance transform. We selected the top- $k$  points from this skeleton, followed by additional distance-based sampling to refine the prompt points.

Clustering algorithms were employed to group spatially connected prompt points into clusters to reduce noise and eliminate false positives. The image was then cropped into smaller batches centered on key regions, with dilation applied to capture critical areas effectively.

Finally, the cropped images were encoded into image embedding using SAM’s image encoder, with the sampled points serving as point prompts. The prompts are turned into prompt embedding using SAM’s prompts encoder.

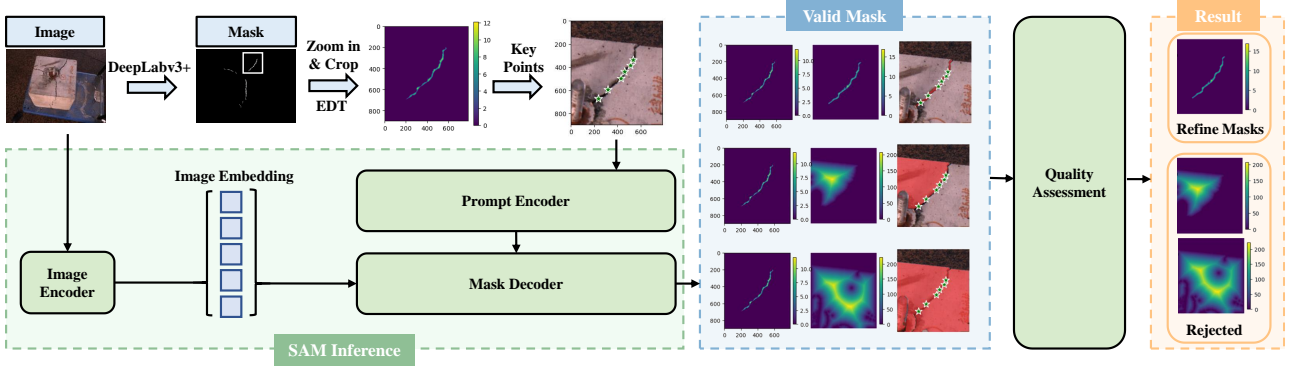


**FIGURE 5** Framework Process for Foundation Model Refinement. The image is first processed using DeepLabv3+ to generate a segmentation mask. This mask is then used to create prompt points for the foundation model, which performs the inference. The results are evaluated for quality, and the optimized mask is selected based on this evaluation.

During SAM inference process the mask decoder will decode refined mask from the image and prompt embeddings.

---

#### Algorithm 1 Perform SAM Inference

---

```

1: procedure SAMINFERENCE(imageBatches)
2:   mask ← DeeplabSegmentation(image)
3:   skeleton ← EuclideanDistanceTransform(mask)
4:   keyPoints ← TopKPoints(skeleton)
5:   sampledPoints ← DistanceBasedSampling(keyPoints)
6:   imageBatches ← ZoomAndCrop(image, sampledPoints)
7:   for batch in imageBatches do
8:     results ← ApplySAM(batch)
9:     promptPoints ← GeneratePrompts(batch)
10:    refinedResults ← RefineResults(results, promptPoints)
11:  end for
12:  qualityScores ← AssessQuality(refinedResults)
13:  finalResults ← RejectPoorResults(refinedResults, qualityScores)
14:  return finalResults
15: end procedure

```

---

- Preprocess:** Convert the result to a binary image  $I_b$  using a threshold value  $T$ :

$$I_b(x, y) = \begin{cases} 1 & \text{if } I_g(x, y) \geq T \\ 0 & \text{if } I_g(x, y) < T. \end{cases} \quad (8)$$

- Inversion:** Invert the binary image  $I_b$  to get  $I_i$ , where holes become foreground (value 1) and the mask becomes background (value 0):

$$I_i(x, y) = 1 - I_b(x, y). \quad (9)$$

- Contour Detection:** Apply a contour detection algorithm on  $I_i$  to find all contours  $C = \{c_1, c_2, \dots, c_n\}$ .
- Hierarchy Analysis:** Analyze the hierarchy of the contours. A contour  $c_i$  represents a hole if it has a parent contour (i.e., it is nested within another contour). Let  $P(c_i)$  denote the parent of the contour  $c_i$ . The number of holes  $H$  is given by the count of contours with a parent:

$$H = \sum_{i=1}^n \mathbb{I}(P(c_i) \neq -1), \quad (10)$$

where  $\mathbb{I}$  is the indicator function, which is 1 if the condition is true and 0 otherwise.

The resulting outputs were then collected for quality assessment, which helped us decide whether to update the initial segmentation results.

### 5.3.2 | Quality Assessment

The result from SAM is not robust due to the inherent randomness of prompts and the contextual semantic complexity within an image. Therefore, a quality assessment and rejection mechanism is proposed to filter out undesired masks based on crack-specific priors related to shape and topology. This mechanism comprises two components: a region size consistency check and a topological consistency check. The size check takes the raw masks and prior knowledge as input to prevent the output from expanding into regions of no interest. The topological check calculates the topological holes inside a mask to avoid one of the common failure patterns of SAM. The steps are as follows:

## 6 | 3D STRUCTURE RECONSTRUCTION

Current crack reconstruction methods, particularly those based on SfM, often produce sparse point clouds with significant noise, leading to suboptimal reconstruction quality. Recent advancements, such as the multi-modal SLAM framework like R3LIVE (Lin and Zhang 2022), have integrated LIO with VIO to enhance reconstruction performance. VIO heavily depends on high camera frame rates (e.g., 120 frames per second in official benchmarks), making it impractical to achieve high image resolutions and the precision required for crack analysis (Feng et al. 2023). Furthermore, VIO struggles to match the performance of LIO with low-frame-rate, high-resolution cameras. To address



these challenges, this study adopts a LiDAR-centric reconstruction framework, emphasizing high-resolution cameras over high frame rates to achieve precise, submillimeter-level crack reconstruction and measurement at comparable costs.

To improve crack reconstruction accuracy and the automation of 3D crack geometric property computation, we have implemented several improvements. First, to address the issue of low point cloud density, the state-of-the-art FastLIO2 (Xu et al. 2022) framework was employed to generate dense point clouds and LiDAR poses. Furthermore, the camera pose was estimated by applying spherical continuous interpolation in the Special Euclidean group ( $SE(3)$ ) based on the computed LiDAR poses. A detailed explanation of this process is provided in Section 6.1. Then, to mitigate the noise in the point clouds, we proposed a two-step approach. The first step involves using the Statistical Outlier Removal (SOR) algorithm to perform coarse noise reduction by removing outliers. In the second step, we applied the MLS algorithm for fine noise reduction and hole filling, achieving more accurate noise removal. A detailed explanation of this process is provided in Section 6.2.

In general, as shown in Step 3 of Figure 1, we first use the FastLIO2 framework to reconstruct a dense point cloud of the crack. Next, the proposed two-stage denoising module is applied to recover the geometry information of the crack by removing outliers, with the specific reconstruction process illustrated in Figure 6.

## 6.1 | Odometry and Reconstruction

To enhance the density of point clouds, this work uses the state-of-the-art SLAM technique, FastLIO2 (Xu et al. 2022), to reconstruct the geometry of the crack.

We begin by deriving the state transition model. The first IMU frame (denoted as  $I$ ) is selected as the global frame, denoted as  $G$ . The known extrinsic transformation between the LiDAR and IMU is represented as  ${}^I T_L = ({}^I R_L, {}^I t_L)$ , where  ${}^I R_L$  and  ${}^I t_L$  denote the rotation and translation between the LiDAR and IMU frames, respectively. The kinematic model can then be formulated as follows:

$$\begin{aligned} {}^G \dot{R}_I &= {}^G R_I [\omega_m - b_\omega - n_\omega]_\wedge, & {}^G \dot{p}_I &= {}^G v_I, \\ {}^G \dot{v}_I &= {}^G R_I (a_m - b_a - n_a) + {}^G g, \\ \dot{b}_\omega &= n_{b_\omega}, & \dot{b}_a &= n_{b_a}, & {}^G \dot{g} &= 0, \\ {}^I \dot{R}_L &= 0, & {}^I \dot{p}_L &= 0, \end{aligned} \quad (11)$$

where  ${}^G p_I$  and  ${}^G R_I$  represent the IMU's position and orientation in the global frame, while  ${}^G g$  is the gravity vector in the global frame. The terms  $a_m$  and  $\omega_m$  denote the IMU's acceleration and angular velocity measurements, respectively, with  $n_a$  and  $n_\omega$  representing the corresponding measurement noise. The IMU biases,  $b_a$  and  $b_\omega$ , follow a random walk process driven by noise terms  $n_{b_a}$  and  $n_{b_\omega}$ . The notation  $[a]_\wedge$  represents the skew-symmetric matrix of a vector  $a \in \mathbb{R}^3$ .

Furthermore, FastLIO2 incorporates an incremental Incremental K-Dimensional Tree (IKD-Tree) (Xu et al. 2022), a dynamic data structure essential for managing the large volumes of point cloud data generated during mapping. The IKD-Tree is an enhanced version of the K-Dimensional Tree

(KD-Tree), supporting incremental updates, which allows it to efficiently process the continuous stream of LiDAR data and generate dense maps without compromising accuracy.

The synergy between the iterative Kalman filter for robust state estimation and the incremental IKD-Tree for efficient map management allows FastLIO2 to deliver accurate LiDAR pose estimation and high-quality point cloud reconstruction in real time.

To accurately estimate the camera pose, we first perform a timestamp alignment between the camera and LiDAR data to synchronize their measurements. With the LiDAR pose already estimated using LIO (Xu et al. 2022), we then use  $SE(3)$  spherical interpolation (slerp) to estimate the camera's  $SE(3)$  pose from the LiDAR pose.

Spherical linear interpolation (slerp) is a method that interpolates between two points on a sphere, providing a smooth transition between poses. Consider two poses represented as rotation matrices or quaternions  $p_0$  and  $p_1$  on the unit sphere. The slerp function smoothly interpolates between these two points as a function of a parameter  $t$  (where  $0 \leq t \leq 1$ ), which controls the interpolation. The  $SE(3)$  interpolation for the pose  $\text{slerp}(p_0, p_1; t)$  is given by:

$$\text{slerp}(p_0, p_1; t) = \frac{\sin[(1-t)\Omega]}{\sin\Omega} p_0 + \frac{\sin[t\Omega]}{\sin\Omega} p_1, \quad (12)$$

where  $\Omega$  is the angle between  $p_0$  and  $p_1$ , computed as:

$$\cos\Omega = p_0 \cdot p_1, \quad (13)$$

with  $\cdot$  representing the dot product between the unit quaternions (or rotation matrices)  $p_0$  and  $p_1$ .

In our context, the poses  $p_0$  and  $p_1$  represent the initial and final LiDAR poses, and  $t$  is the normalized time parameter corresponding to the camera timestamp within the LiDAR sequence. The result of the slerp function gives us the interpolated camera pose  $\text{slerp}(p_0, p_1; t)$ , which is a smooth interpolation between the two LiDAR poses.

According to the above method, the schematic diagrams of reconstruction results are shown in Figure 6a and Figure 6e.

## 6.2 | Denoise

To decrease the noise of the reconstruction map generated from Section 6.1, we applied a denoising and smoothing post-processing module to enhance the quality of the reconstructed map. The denoising module contains two-stages, it begins with the SOR filter, which is implemented using the Point Cloud Library (PCL) and assumes that the distance between a given point and its neighbors is normally distributed (Balta et al. 2018). In the second stage, the MLS method is employed to smooth and refine the point cloud.

In the SOR filter, for each point  $p_i$  in the dataset, the average distance  $r_i(K)$  to its  $K$  nearest neighbors (KNN) is computed. This value is then assessed using the sigma rule across the entire dataset, where points whose average distance does not fall within  $N$  standard deviations from the mean are classified as outliers and removed. The default parameters typically used are  $K = 60$  and  $N = 1$ , which effectively removes noise while preserving the integrity of the data. Mathematically, the outlier condition can be expressed as:

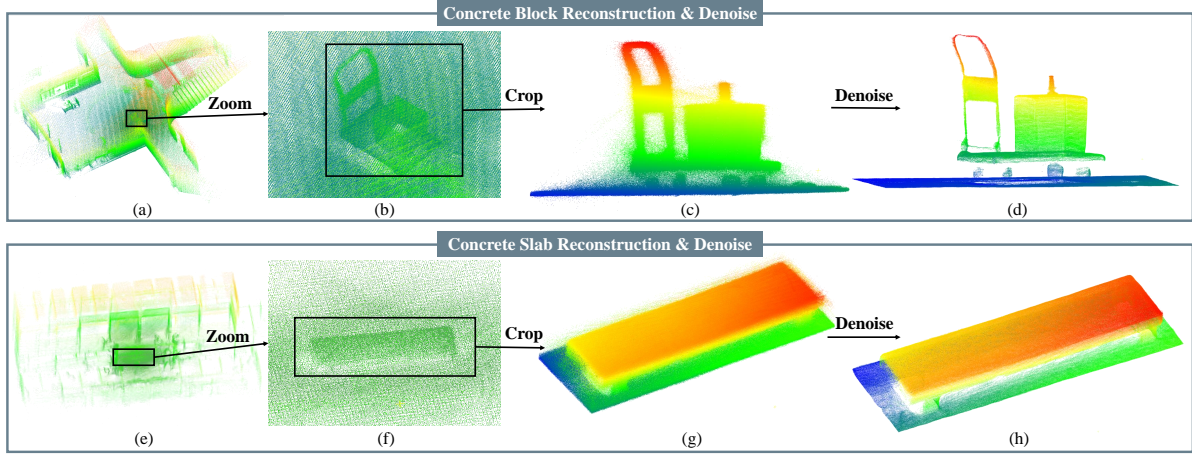


**FIGURE 6** 3D Reconstruction Process. (a) - (d) and (e) - (h) illustrate the reconstruction, cropping, and point cloud denoising processes using MLS and SOL for the concrete block and concrete slab, respectively.

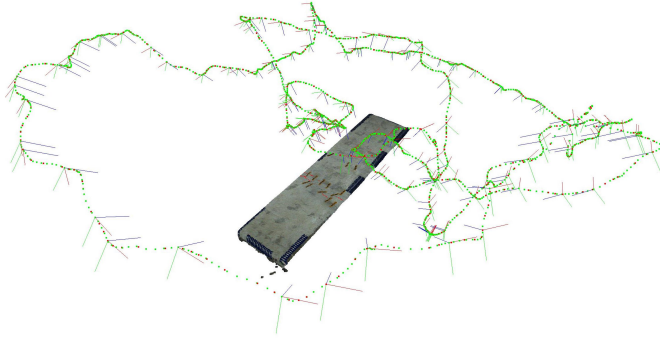


**FIGURE 7** Data Collection Trajectory. The green points represent the Lidar-recorded poses, while the red points indicate the estimated camera poses.

$$\text{Outlier Condition: } r_i(K) > \mu_r + N \cdot \sigma_r, \quad (14)$$

where  $\mu_r$  and  $\sigma_r$  are the mean and standard deviation of the average distances  $r_i(K)$  across all points in the dataset. By choosing the appropriate value  $N$ , the filter can be tuned to balance the removal of outliers with the retention of legitimate data points. Here we set  $N = 1$  which ensures that approximately 68.27% of inliers are retained, according to the cumulative distribution function (CDF) of the normal distribution.

After applying the SOR filter, we employ the MLS method, which is a powerful technique used to reconstruct continuous functions from a set of unorganized point samples by calculating a weighted least squares approximation that emphasizes regions near the point of interest (Ahn et al. 2005).

Formally, consider a function  $f : \mathbb{R}^n \rightarrow \mathbb{R}$  and a set of sample points  $S = \{(x_i, f_i) \mid f(x_i) = f_i\}$ . The MLS approximation  $\tilde{p}(x)$  of degree  $m$  at a point  $x$  is defined as the polynomial  $\tilde{p}(x)$  that minimizes the weighted least-squares error:

$$\tilde{p}(x) = \arg \min_p \sum_{i \in I} [p(x_i) - f_i]^2 \theta(\|x - x_i\|), \quad (15)$$

where  $p(x)$  is a polynomial of degree  $m$  in  $\mathbb{R}^n$ , and  $\theta(\|x - x_i\|)$  is a weighting function that decreases as the distance between  $x$  and  $x_i$  increases. Our choice for the weighting function is the Gaussian function:  $\theta(s) = e^{-s^2}$ , which ensures that points closer to  $x$  have a greater influence on the polynomial fit than points farther away. The polynomial  $\tilde{p}(x)$  is then used to project each point in the point cloud onto the locally approximated surface, resulting in a smoother and denser point cloud.

The combination of the SOR method for outlier removal followed by the MLS method for surface smoothing ensures that the resulting point cloud is both accurate and visually coherent. Based on this denoising approach, the concrete portions of the reconstructed structure, of interest, were extracted, as shown in Figures 6c and 6g. The denoised results are presented in Figures 6d and 6h. This provides a high-quality foundation for subsequent tasks, including point cloud coloring, crack segmentation, and the computation of crack 3D geometric properties.

## 7 | QUANTIFICATION OF CRACK SIZE AND LOCALIZATION

This chapter focuses on extracting the geometric properties of concrete cracks derived from 3D reconstruction results. The key challenges are: (1) how to integrate multi-frame crack image information into the overall 3D point cloud data structure (2) how to automate the calculation of crack 3D geometric properties, including crack width, specific location, distribution, and orientation. To address these challenges, a multi-frame and multi-modal fusion framework is proposed in Section 7.1, which enables the construction of a colored point cloud model with geometric 3D crack information. In Section 7.2, an automated framework is introduced to measure crack properties, enabling precise quantification and localization of crack width.

## 7.1 | Multi-Frame & Multi-Modal Fusion

To integrate multi-frame crack image information into the overall 3D point cloud data structure, the key challenge lies in resolving the misalignment between image pixels and the point cloud. To address this problem, a multi-frame and multi-modal fusion approach was adopted, as shown in Figure 8. For each 3D point, all camera frames that observed it over time were identified. The color values from these frames were then ranked and weighted. Subsequently, the color values from different frames were smoothed to obtain an optimized color value for each 3D point. In addition, to enhance the accuracy of camera pose estimation, slerp in the  $SE(3)$  group was used to estimate the camera pose. This approach can be divided into several key stages, as described below.

1. **Transforming the Point Cloud to Camera Coordinates:** For each image frame, the point cloud is transformed into the camera coordinate system using the camera's pose, which has been estimated via  $SE(3)$  spherical interpolation (Pennec 1998), and the extrinsic calibration parameters between the LiDAR and the camera. The transformation is mathematically represented in Eq (1).

2. **Visibility Filtering Using the Hidden Point Removal (HPR) Operator:** Before projecting the LiDAR points onto the camera's image plane, we need to determine which points are visible from the current camera viewpoint. This is accomplished using the Hidden Point Removal (HPR) operator (Katz et al. 2007), which efficiently filters out points that are occluded from the camera's view.

The HPR operator works in two main steps: inversion and convex hull construction. First, each point  $\mathbf{P}_i \in P$  is transformed with respect to the camera position  $C$  using spherical inversion:

$$\hat{\mathbf{P}}_i = \mathbf{P}_i + 2(R - \|\mathbf{P}_i\|) \frac{\mathbf{P}_i}{\|\mathbf{P}_i\|}, \quad (16)$$

where  $R$  is the radius of a sphere centered at the camera position  $C$ , and  $\|\mathbf{P}_i\|$  is the distance of  $\mathbf{P}_i$  from  $C$ . This transformation reflects each point with respect to the sphere, moving it to a position outside the sphere.

After inversion, the convex hull of the transformed point cloud  $\hat{P} = \{\hat{\mathbf{P}}_i\}$  combined with the camera position  $C$  is computed. A point  $\mathbf{P}_i$  is considered visible if its transformed point  $\hat{\mathbf{P}}_i$  lies on the convex hull of  $\hat{P} \cup \{C\}$ . This approach ensures that points occluded by others are effectively filtered out, leaving only those visible from the camera.

3. **Projecting Visible LiDAR Points onto the Camera Image Plane:** The filtered LiDAR points, determined to be visible using the HPR operator, are then projected onto the camera's image plane using the camera's intrinsic parameters. The projection from 3D camera coordinates  $\mathbf{P}_C = [X_C \ Y_C \ Z_C]^T$  to 2D pixel coordinates  $\mathbf{p}_{uv} = [u \ v]^T$  is given by:

$$\mathbf{p}_{uv} = \mathbf{K} \begin{bmatrix} X_C/Z_C & Y_C/Z_C & 1 \end{bmatrix}^T, \quad (17)$$

where  $\mathbf{K}$  is the camera intrinsic matrix. The corresponding color information from the image at these pixel coordinates is then associated with the 3D point.

4. **Accumulating and Optimizing Color Information:** As the process iterates over all image frames, each point in the point cloud model

accumulates color information from multiple views. For each point, color data from  $N$  frames is collected, where  $N$  ranges from 0 to the total number of frames. This redundancy is crucial for achieving a robust and accurate colorization of the point cloud.

5. **Scoring and Weighting Frames to Select Optimal Views:** To select the optimal color information for each point, a weighted scoring method is introduced based on two criteria:

- **Orientation Score:** This score reflects the alignment between the point-to-camera vector and the camera's viewing direction. It is computed as:

$$\text{Score}_1 = \cos(\theta) = \frac{\mathbf{D}_{\text{point to cam}} \cdot \mathbf{N}_{\text{cam plane normal}}}{\|\mathbf{D}_{\text{point to cam}}\| \|\mathbf{N}_{\text{cam plane normal}}\|}, \quad (18)$$

where  $\mathbf{D}_{\text{point to cam}}$  is the vector from the camera to the point, and  $\mathbf{N}_{\text{cam plane normal}}$  is the normal vector of the camera's image plane.

- **Distance Score:** This score penalizes points based on their distance from the camera, favoring points close to the ideal distance (e.g., 2 meters) for accurate color capture. The score is given by:

$$\text{Score}_2 = \exp\left(-\frac{(\|\mathbf{D}_{\text{point to cam}}\| - 2)^2}{2\sigma^2}\right), \quad (19)$$

where  $\sigma$  controls the spread of the distance penalty.

The final weight for each frame is calculated as a combination of these two scores:

$$w_i = \lambda_1 \cdot \text{Score}_1 + \lambda_2 \cdot \text{Score}_2, \quad (20)$$

where  $\lambda_1$  and  $\lambda_2$  are weighting factors that balance the importance of orientation and distance.

6. **Fusing Color Information from Top Views:** For each 3D point, the top  $N$  frames with the highest weights are selected as the best views. The RGB color from these frames is fused to determine the final color of the point using the normalized weights:

$$\text{Color}_{\text{final}} = \frac{\sum_{i=1}^N w_i \cdot \text{Color}_i}{\sum_{i=1}^N w_i}. \quad (21)$$

This approach ensures that the final color assigned to each 3D point is derived from the most reliable and accurately captured views, leading to a high-quality, colorized point cloud model.

The proposed method not only denoises and smooths the point cloud model but also enhances it with precise and vivid color data, increasing its visual quality and utility across diverse applications. Moreover, the integration of fusion images, masks, and the reconstruction model enables accurate restoration of the concrete structure's color and detailed semantic representation of cracks in 3D, facilitating subsequent automatic crack geometric property measurements. By employing the above method, fusion images, masks, and the reconstruction model can yield a model that accurately restores the color of the concrete structure and the semantic information of the cracks with true 3D dimensions.

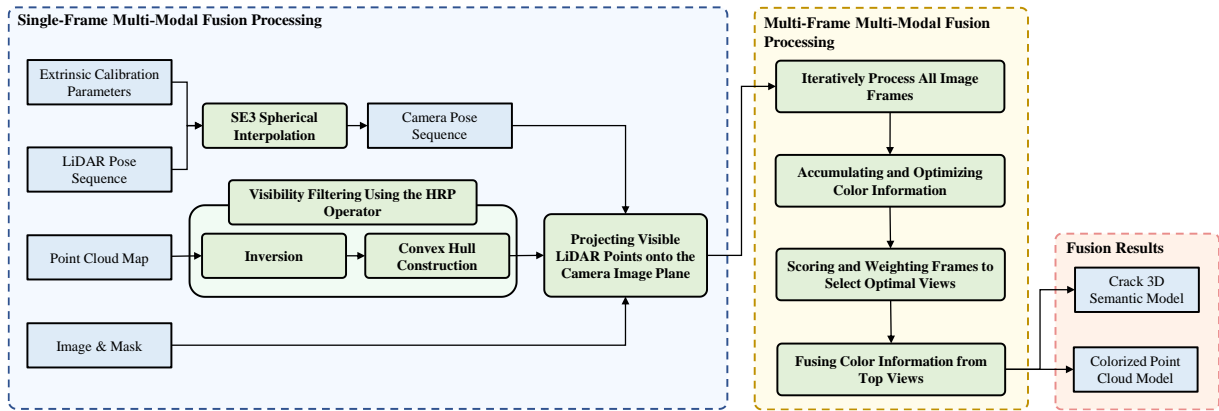


**FIGURE 8** Framework process for multi-frame and multi-modal fusion of point cloud and image data. The point cloud is first transformed to camera coordinates, and visible points are filtered using the HPR operator. These points are then projected onto the image plane, where color information from multiple frames is accumulated. Finally, the optimal color is selected and fused from the top frames to create a high-quality, colorized 3D point cloud.

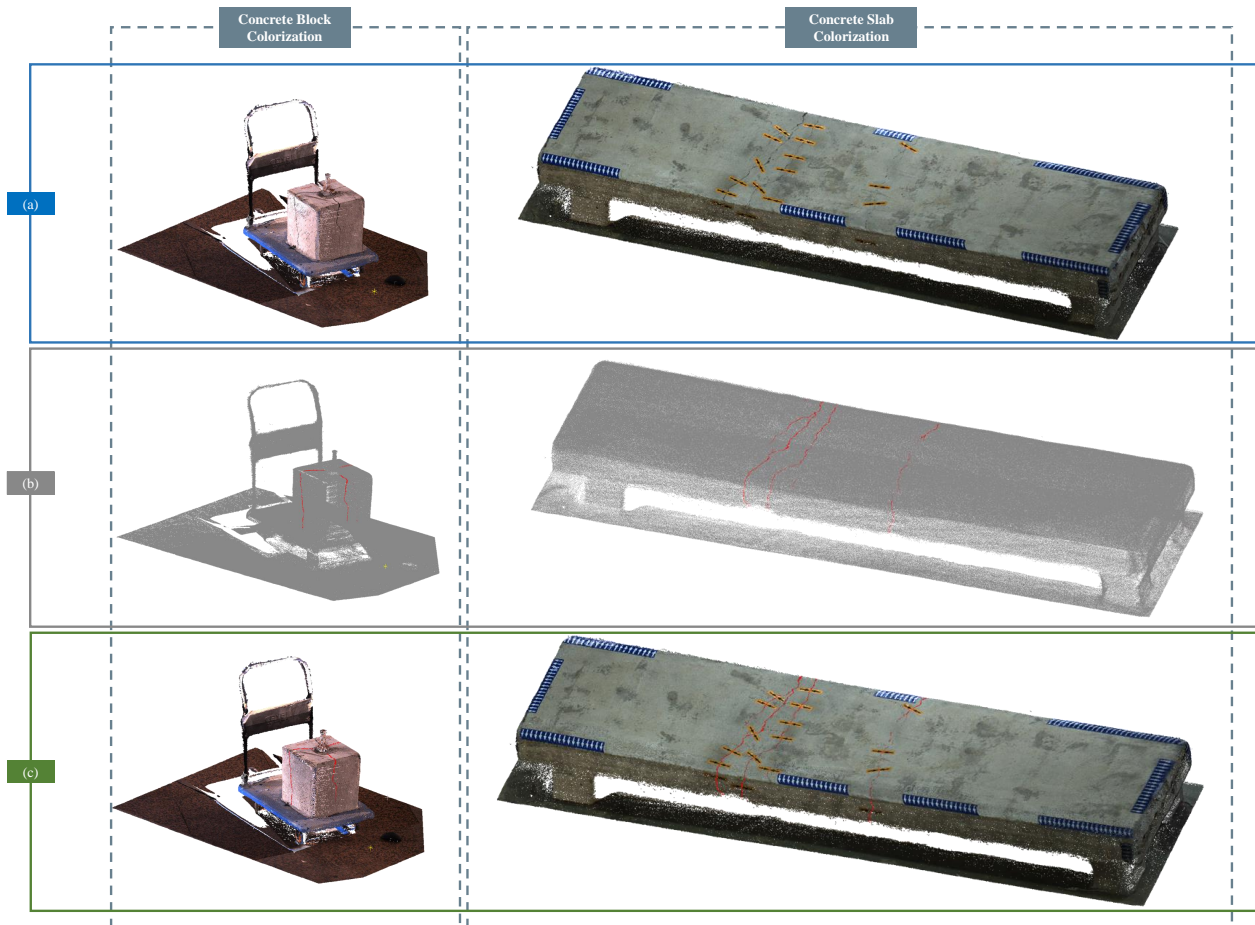


**FIGURE 9** Results of Multi-Frame and Multi-Modal Fusion. (a) is the colorized 3D point cloud model, representing the fusion of point clouds and images; (b) is the crack-segmented 3D point cloud model, representing the fusion of point clouds and masks; (c) is the colorized and crack-segmented 3D point cloud model, representing the combined result of (a) and (b).

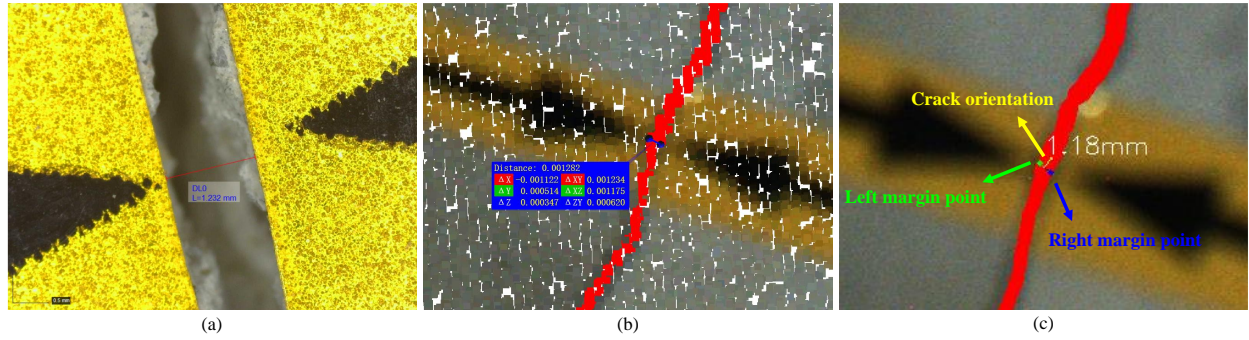


**FIGURE 10** (a) Control Test: Results measured with a Dinolite microscope. (b) Direct Measurement: Two points are measured directly within the point cloud. (c) Automatic Measurement: The 3D coordinates of the left and right edge points of the crack (represented by the green and blue dots in the graph) at the measured position are automatically identified based on the crack skeleton. The 3D distance between the two points is then calculated using their absolute 3D coordinates.

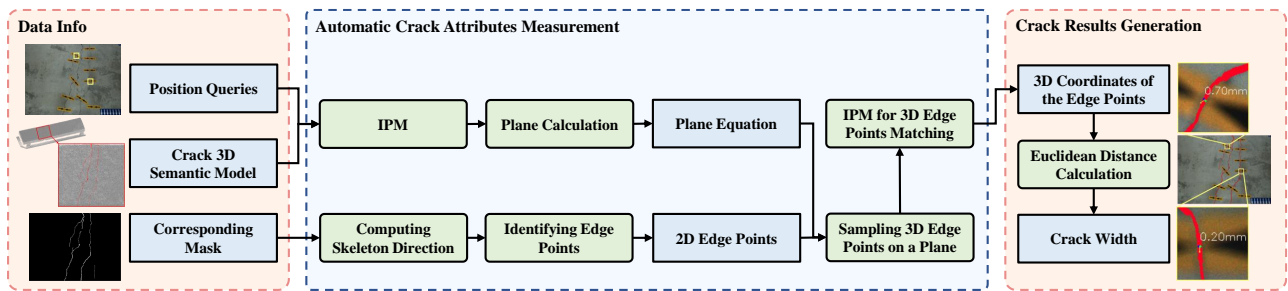


**FIGURE 11** Framework process for automatic crack width measurement and crack localization. The workflow begins by selecting the crack location on the image, from which the crack orientation and boundary points are computed. These boundary points are then back-projected onto the 3D point cloud model to obtain their true 3D coordinates. The 3D distance between the boundary points is calculated to determine the crack width, ensuring accuracy and objectivity in the measurement. This method automates the crack width calculation and provides precise 3D positional data of the cracks.

## 7.2 | Automatic Measurement of Crack Geometric Properties

Once the 3D model, with real-world dimensions and crack segmentation point clouds, is obtained, as shown in Figure 10b, it becomes straightforward to directly measure the width of cracks by selecting two edge points from the 3D point cloud.

However, manually identifying the two edge points of the crack makes the method inherently subjective. Additionally, when measuring the width of multiple cracks, the workload increases significantly. Moreover, this method typically calculates crack widths by analyzing relative coordinate differences in single-frame point clouds (Hu et al. 2024). However, it is restricted to crack width measurements and cannot provide precise three-dimensional crack positions in a unified coordinate system. Therefore, automating crack width measurement while integrating precise 3D positional data remains a significant challenge.

To address this, we propose a workflow that combines crack segmentation masks with 3D reconstruction data to automatically compute key crack attributes, including width and precise 3D position. The proposed automatic crack width measurement method eliminates the need for manually selecting edge points. Instead, the crack location is simply identified on the image and the crack



direction and boundary points are then automatically calculated. These points are inverse-projected onto the 3D point cloud model to obtain the true 3D coordinates of the boundary points. The 3D distance between boundary points is then computed, ensuring objective measurement. This method not only enables automatic crack width measurement but also provides accurate 3D location data for the measured cracks. As shown in Figure 11, the core steps of the algorithm for maintaining the accuracy of the 3D crack information are as follows:

1. **Computing Skeleton Direction:** To estimate the direction of a crack at a given point on a 2D skeleton image, a local neighborhood around the point is first extracted, followed by Gaussian smoothing to reduce noise. The direction vector is determined by calculating the gradients within this neighborhood using the Sobel operator. The average gradient is then computed, which provides the direction vector, subsequently normalized.
2. **Identifying Edge Points:** Upon computation of the direction vector, it is used to trace the crack edges. By following the direction and its perpendicular vectors, the left and right edge points relative to the skeleton point are located. This tracing is performed iteratively until the crack edge is fully detected.
3. **Sampling 3D Points on a Plane:** To ensure accurate 3D reconstruction of crack edges, points are sampled on a plane defined by the coefficients  $(a, b, c, d)$  of the plane equation. Given a center point  $(x_0, y_0, z_0)$  on the plane, a grid of  $x$  and  $y$  coordinates is generated within a specified radius, and the corresponding  $z$  values are computed using the plane equation:

$$z = \frac{-ax - by - d}{c}. \quad (22)$$

This process results in a set of 3D points sampled across the plane.

4. **Searching for 3D Edge Points:** The sampled 3D points are projected onto the 2D image plane using the camera's intrinsic parameters. By comparing the projected points with the observed edge points in the image, the 3D points corresponding to the actual crack edges are identified. The 3D point that best matches the observed edge is selected based on the minimum projection error.
5. **Calculating Crack Width:** The crack width is determined as the Euclidean distance between the identified left and right edge points in 3D space.

The described pipeline enables the accurate capture and computation of crack width, thereby facilitating a comprehensive analysis and quantification of cracks within the point cloud domain, which achieves the synchronous measurement of crack width and its three-dimensional positional information.

## 8 | EXPERIMENTAL SETUP

### 8.1 | Platforms

This study introduces a state-of-the-art 3D reconstruction system based on SLAM technology, specifically designed for the detection and reconstruction of cracks in concrete structures. By seamlessly integrating LiDAR and visual data, the system significantly improves data accuracy, enabling precise crack

**TABLE 1** Main parameters of equipment.

Equipment	Type	Specification
LiDAR	Hesai XT32-M2X	FOV: $360^\circ \times 40.3^\circ$ Angular Resolution: $0.18^\circ \times 1.3^\circ$ Range Precision: 0.5 cm ( $1\sigma$ ) Ranging Capability: 0.5–300 m Resolution: $4096 \times 3000$
Camera	HikRobot MV-CH120-10GC	
Lens	HikRobot MVL-KF1628M-12MPE	Focal length: 16 mm
IMU	WitMotion 9-axis IMU HWT905	Accuracy: $0.05^\circ$

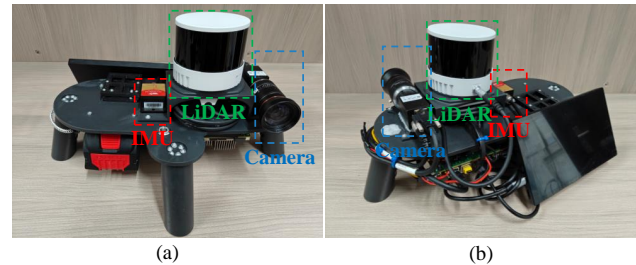


**FIGURE 12** Experimental setup, where one Hesai XT32-M2X LiDAR, one IMU and one HikRobot camera are utilized for data acquisition.

measurement and efficient 3D reconstruction in real time. To facilitate real-world applications, we developed a handheld device (Figure 12) equipped with a global shutter camera and lens, a LiDARs listed in Table 1

The LiDAR captures precise point-cloud data while the camera is utilized for high-resolution image acquisition. The LiDAR captures precise point-cloud data. The IMU records the high-frequency motion changes of the device, and the industrial computer coordinates system operations and stores the collected data. This integration of components ensures both precision in crack quantification and the robustness of the 3D reconstruction process. The device is powered by an Intel i7-1265UE CPU with 32 GB of RAM and an integrated power supply.

### 8.2 | Model Implementations

The crack segmentation on images and the process of 3D reconstruction were conducted on a computing platform running the Ubuntu 22.04 LTS system, equipped with an Intel i9 13900K processor with 128.0 GB RAM and an NVIDIA RTX 4090 graphics card with 24.0 GB VRAM. All deep learning frameworks were implemented using PyTorch 2.0.0 with CUDA 11.5.119. For the segmentation model, the training process is divided into two stages: pre-training and fine-tuning. For pre-training, ten open-source datasets as listed in Table 2 were integrated and divided into training and validation sets in an 8:2 ratio. The batch size for the pre-training phase was set to 32, with an initial learning rate of 0.01, and the number of iterations was set to 50. The model with the best performance was selected as the pre-trained model. For fine-tuning, the self-annotated dataset was split into training and testing subsets with a 7:3 ratio. The fine-tuning process used a batch size of 3, an initial learning rate of 0.001, and ran for a total of 200 iterations. Following inference using the pre-trained





**FIGURE 13** Data Collection Objects: (a) and (b) show the overall and local views of the concrete slab, respectively, while (c) and (d) show the overall and local views of the concrete block.

**TABLE 2** Dataset List. This table presents the source and size of both our pre-training and experimental datasets.

Crack Dataset	Size	Resolution
Ceramic-Cracks	100	256×256
CFD	118	480×320
Crack500	50	400×400
CrackTree200	206	800×600
DeepCrack	527	544×384
GAPS	544	1920×1080
Masonry	240	224×224
Rissbilder	5591	448×448
Volker	990	448×448
CCSS-DATA	670	544×384
Our dataset	150	4096×3000

and fine-tuned models, segmentation results were further enhanced through a refinement process utilizing SAM models. Additionally, to mitigate the effects of overfitting, data augmentation techniques such as random horizontal and vertical flips, random rotations, and Gaussian blurring were employed during the training process.

### 8.3 | Crack Segmentation Datasets

The experimental dataset used in this work comprises 10 open-source datasets, as detailed in Table 2. This dataset contains 9,260 RGB images of varying sizes captured in diverse environments, all annotated at the pixel level for cracks. The cracks include three material types: concrete structural cracks, asphalt pavement cracks, and ceramic cracks. Such a multi-scale, multi-scenario dataset enhances the model's ability to generalize across different crack sizes and materials, improving robustness in varied environments.

The training and testing sets for unseen scenarios were derived from images captured in this study's experimental setup using a handheld device. These images were manually annotated with the PixelAnnotationTool (Br  h  ret 2017) and subsequently split into training and testing sets in a 7:3 ratio. These images have a pixel resolution of 4096 by 3000 and exhibit different shooting angles, distances, and blurriness. The dataset also contains artifacts such as reflective tags, shadows, stains and environmental objects.

### 8.4 | Data Acquisition from Field Experiments

The effectiveness of the proposed system for crack detection, localization, and width measurement was validated through experiments conducted on a concrete block and a walking slab (reinforced concrete slab) taken from the sides of an actual railway bridge. The experimental subjects are shown in Figure 13. Figure 13a illustrates the concrete block specimen, which is a standard cube with dimensions of 300mm × 300mm × 300mm, placed on a trolley. Cracking occurred due to bolt pull-out, as shown in Figure 13b. In Figure 13c, the concrete slab is positioned in a laboratory with a complex environment. The cracks that developed during the loading process are mainly located at the center of the slab, with dimensions of 1580mm × 300mm × 80mm.

During data collection from the concrete slab, a self-developed handheld device with a camera, as described in Section 8.1, was directed at the concrete slab. The data were recorded by rotating around the slab in a counterclockwise direction, with the image capture path depicted in Figure 7. During data recording, the laser point cloud was collected at 10 Hz, IMU data at 200 Hz, and images at approximately 5 Hz. The total recording time was about 2 minutes. The same procedure was used for collecting data from the concrete cube specimen. Additionally, to verify the feasibility of the crack width measurement method, four major cracks were selected on the concrete slab. These cracks traversed all four faces of the slab. At intervals of approximately 10 mm along the crack direction, the actual crack width was measured using a Dino-Lite AF4915 microscope. The measured values were then compared with the 3D crack width information obtained by the proposed method. To facilitate the matching of the actual crack measurements with the corresponding locations in the 3D reconstruction results, yellow reflective markers were placed at the measurement points, as shown in Figure 13d.

In subsequent experiments, as shown in Figure 15b, although the yellow reflective markers significantly affected the segmentation results of the baseline model, the Foundation Model Refine Process maintained excellent segmentation performance. This enabled the automated crack width measurement results to retain submillimeter-level accuracy, demonstrating the robustness of the proposed method. This will be fully demonstrated in Sections 9.1 and 9.2. The treatment of the concrete cube specimen followed the same procedure.

**TABLE 3** Foundation Model Refine Results. This table shows the improvement in segmentation performance achieved by our optimization method across various models and shot numbers.

# Shots	Method	mIOU (%)	
		Baseline	Refined ( <i>Ours</i> )
0	Swit-Transformer	36.77	44.15 (+7.38)
	TernausNet	42.13	49.92 (+7.79)
	TransUnet	45.28	52.04 (+6.76)
	DeepLabv3+	46.61	53.21 (+6.60)
10	Swit-Transformer	41.29	45.59 (+4.30)
	TernausNet	45.51	50.83 (+5.32)
	TransUnet	49.77	53.55 (+3.78)
	DeepLabv3+	50.13	55.27 (+5.14)
110	Swit-Transformer	50.01	54.73 (+4.72)
	TernausNet	57.24	59.18 (+1.94)
	TransUnet	60.38	61.30 (+0.92)
	DeepLabv3+	61.41	62.25 (+0.84)

**TABLE 4** Automatic Crack Width Measurement Results. This table compares the crack width measurements from our method with those obtained using the microscope.

Crack ID	Calculated Value (mm)	Reference Value (mm)	Absolute Error (mm)	Relative Error (%)
#1	0.59	0.65	0.06	9.09
#2	0.86	0.91	0.05	5.49
#3	0.38	0.56	0.18	32.26
#4	1.18	1.23	0.05	4.22
#5	0.96	0.92	0.04	4.80
#6	1.72	1.43	0.29	20.11
#7	0.66	0.67	0.01	1.49
#8	0.40	0.58	0.18	30.80
#9	0.30	0.45	0.15	33.92
#10	0.20	0.29	0.09	30.56
#11	0.75	0.86	0.11	12.28
#12	1.41	1.49	0.08	5.24
#13	0.32	0.28	0.04	15.94
#14	0.85	0.91	0.06	6.80
#15	0.51	0.52	0.01	2.49
<b>Mean Error</b>			0.09	14.37

## 9 | EXPERIMENTAL RESULT

### 9.1 | Results of Image Crack Segmentation

Mean Intersection over Union (mIoU) is a prevalent evaluation criterion for semantic segmentation. IoU refers to the ratio of intersection and union between the predicted target area and the real target area. mIoU is the average of IoU for all classes. mIoU is calculated as follows:

$$mIoU = \frac{\left( \sum_{i=1}^N \frac{X_{ii}}{\sum_{j=1}^N X_{ij} + \sum_{j=1}^N X_{ji} - X_{ii}} \right)}{N}, \quad (23)$$

where  $N$  is the number of classes including background,  $X_{ii}$  represents the number of pixels correctly recognized as class  $i$ ,  $X_{ij}$  represents the number of pixels recognized as class  $j$  but actually class  $i$  and  $X_{ji}$  represents the number of pixels recognized as class  $i$  but actually class  $j$ .

In addition, DeepLabv3+ (Chen et al. 2018), TransUnet (Igllovikov and Shvets 2018), Swin-Transformer (Liu et al. 2021c), and TernausNet (Igllovikov

and Shvets 2018, Pantoja-Rosero et al. 2022) were selected for comparison along with our foundation model refinement method. This comparison was conducted to assess the segmentation performance of refinement by SAM across different baselines. In practical engineering structure damage detection, crack image segmentation tasks often require the segmentation model to perform pixel-level segmentation of concrete cracks in diverse environments. To meet these demands, the performance of the networks was evaluated and compared under zero-shot, 10-shot, and 110-shot conditions. Furthermore, the SAM-refined results demonstrated substantial improvements in the generalization ability of SAM, particularly across novel scenarios and varied model architectures.

Four crack segmentation networks were trained on the training set and evaluated on the test set. The results were compared to assess performance improvements due to refinement. Table 3 presents the IoU values before and after refinement. Notably, the combination of DeepLabv3+ with SAM refinement achieved the highest IoU score. The results of the selected DeepLabv3+ model combined with SAM refinement on the test set are shown in Figure 15. To make the refinement effects clearer, all the images in Figure 15 are local

**TABLE 5** Reconstruction Results for Different Methods. This table compares the performance of the SOTA and proposed methods in terms of point cloud quality, geometric accuracy, efficiency, and applicability for on-site crack inspection.

Evaluation Metric	COLMAP	LOAM	Ours
<b>Point Cloud Quality <sup>1</sup></b>			
Point Surface Density (number) $\uparrow$	165,208.47	1,471,886.13	3,173,144.75
Point Surface Density (r=10mm) Std. Dev $\uparrow$	26,907.36	710,970.51	992,057.63
Surface Roughness (%) $\downarrow$	0.0279	0.1556	0.0494
Surface Roughness (r=10mm) Std. Dev $\downarrow$	0.000367	0.001223	0.000390
<b>Geometry Accuracy</b>			
Geometric Dimension (mm)	N/A	393.9	380.5
Mean Error(%) $\downarrow$	N/A	3.66	0.13
<b>Efficiency</b>			
Offline Computational time (min) $\downarrow$	300.32	11.2	35.13
<b>On-site Crack Inspection</b>			
Sensor Types	Camera	LiDAR & IMU	Camera & LiDAR & IMU
Real-time Sparse Reconstruction	No	Yes	Yes

<sup>1</sup> Point Cloud Density refers to the number of adjacent points within a 10 mm radius around each point on average.



**FIGURE 14** Field Operation for Concrete Slab: This figure illustrates the data collection process for the concrete slab, along with the corresponding data. It also shows the measurement of crack true values using a Dino-Lite AF4915 microscope.

images cropped from the original images captured by the device. SAM significantly enhances segmentation performance in complex scenarios, including concrete images with crack-like interference, overexposed images, branching or inclined cracks, fine cracks smaller than 3 pixels, label-occluded cracks, and images with surface stains. Its enhancement is particularly evident in zero-shot and 10-shot settings. The introduction of the foundation model SAM significantly enhances the robustness of crack image segmentation, thereby improving the continuity of the segmentation results. Overall, compared to traditional methods, our approach innovatively transforms this task into a two-stage segmentation-enhancement framework. By converting the suboptimal results of the base model into prompts, we effectively leverage the capabilities of the foundation model in the second stage. This enables us to achieve robust segmentation performance while significantly reducing the reliance on annotated data. From an engineering perspective, this significantly enhances the method's generalizability and robustness while reducing the implementation cost in new scenarios. In subsequent field experiments, the trained DeepLabv3+ model served as the base crack segmentation model.

## 9.2 | Results of 3D Crack Localization and Automated Crack Width Measurement

This section presents the reconstruction results from the field inspection experiments.

The reconstruction process commenced utilizing the methodology delineated in Section 6. The specific workflow for 3D point cloud reconstruction and processing is depicted in Figure 6. The point cloud generated by SLAM forms a large-scale scene reconstruction of complex environment. To obtain the specific reconstruction results for the concrete specimens, the point cloud model was cropped to a required size. It was then filtered and smoothed using SOR and MLS, resulting in a denoised output. After obtaining the reconstructed point cloud model, the multi sensor data fusion is performed in a self-synchronous mode, using the method described in Section 7.1. A subset of frame images is automatically selected as key frames, and the images are projected onto the reconstructed point cloud for coloring based on the computed image poses. The resulting colored point cloud is shown in Figure 9a. Similarly, mask images were projected onto the point cloud based on their corresponding image poses to segment and color the point cloud (fusion), producing a 3D point cloud with crack segmentation information, as illustrated in Figure 9b. The colored point cloud shown in Figure 9a was integrated with the segmented point cloud in Figure 9b to merge semantic information, culminating in a 3D concrete model with crack semantic information and coloring, as demonstrated in Figure 9c. This process achieved the 3D localization of crack semantic information.

Once the 3D concrete model with crack semantic information and coloring was obtained, crack width measurements were automatically conducted on 15 cracks marked with yellow labels, as described in Section 7.2. Table 4 presents a comparison between the crack widths measured by a microscope and the calculated results from the proposed framework. Among the detected cracks, the maximum relative error was 33.92%, for Crack ID #9, which had a measured width of only 0.45 mm, with an absolute error of just 0.15 mm. For Cracks #3, #8, #9, #10, and #13, where the crack width was less than 0.5 mm, although the relative errors were larger, the absolute errors were all within 0.2 mm. The significant relative error is due to smaller crack widths,

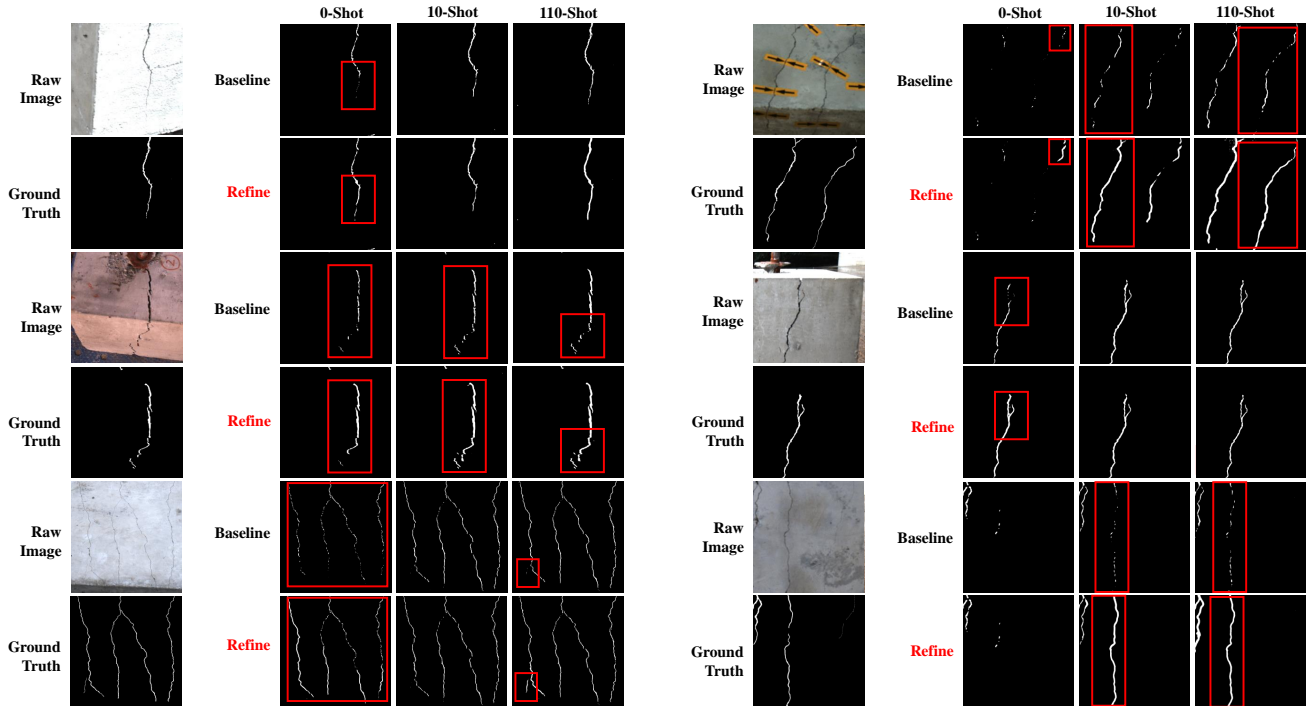


FIGURE 15 A qualitative performance comparison between the baseline model and a version enhanced through foundation model refinement on the task of crack segmentation.

which yield lower reference values for comparison. Accumulated factors such as pixel segmentation errors, SLAM localization inaccuracies, algorithmic deviations, and projection errors collectively contribute to an absolute error of approximately 0.1 mm, which amplifies the relative error.

Overall, the proposed framework demonstrated an average absolute error of less than 0.1 mm and an average relative error of less than 15%, sufficiently validating the framework's applicability for crack measurement in practical engineering applications.

### 9.3 | Comparative Analysis of 3D Reconstruction Methods

To further analyze the outstanding advantages of the proposed framework in terms of accuracy and robustness for 3D reconstruction, a comparison was made between our multi-sensor fusion-based SLAM method and two traditional approaches, using the same dataset. These include the SfM method (compared using COLMAP software) and the LiDAR SLAM-based LOAM method. The comparisons were made based on geometric accuracy, point cloud resolution, point cloud surface roughness, field operation efficiency. The comparison results are presented in Table 5.

1. **Geometric Size Measurement:** The accuracy of the 3D model is crucial for the precise localization and measurement of cracks. This accuracy can be evaluated by determining the point-to-point distance between selected feature pairs. For this purpose, the width of a concrete slab was chosen as the geometric feature for distance measurement, with manual

measurements serving as the ground truth to calculate the relative size errors of the three methods. As shown in Table 5, the SfM method does not incorporate actual scale during the reconstruction process, rendering the geometric error inapplicable. The proposed framework demonstrated higher accuracy in reconstruction compared to the LOAM method, achieving submillimeter precision.

2. **Point Cloud Resolution:** The resolution of the point cloud determines the minimum crack size that can be detected and measured by the proposed method. This can be evaluated by calculating the average and standard deviation of the number of points within a 10 mm radius around each point. In monocular camera-based reconstruction workflows, the point cloud resolution is largely dependent on image resolution. The LOAM method, lacking a camera, is unable to identify semantic information related to cracks within the point cloud. In the proposed method, point cloud resolution is primarily dependent on the LiDAR resolution. A comparison of the reconstruction results is shown in Figure 16, and Table 5 highlights the significant advantage of the proposed method over other methods in terms of point cloud quality.
3. **Point Cloud Surface Smoothness:** The roughness of the point cloud is measured by the distance between each point and the best-fit plane calculated from its nearest neighbors, reflecting the consistency of the 3D reconstruction quality. This metric also affects the accuracy of crack size measurements obtained from the point cloud. As shown in Table 5, the average point cloud surface smoothness and standard deviation of the proposed method are similar to those of the SfM method.





**FIGURE 16** Comparison of 3D reconstruction results from different perspectives and reconstruction details between our method and the SfM-based COMLAP method. The results were analyzed from multiple viewpoints to assess the overall reconstruction quality, detail accuracy, and robustness of each method.

4. **On-site Efficiency:** In field operations, the proposed method facilitates easy acquisition of sensor data, demonstrating higher inspection efficiency compared to traditional methods. In terms of reconstruction time, as shown in Table 5, the integration of LiDAR and IMU sensors enables real-time 3D reconstruction on-site. This capability significantly reduces the risk of reconstruction failure and minimizes the need for rework due to unsuccessful image alignment. In contrast, the SfM method requires high photo overlap during data collection to ensure successful reconstruction, which imposes stringent requirements on data acquisition conditions. Particularly in real-world engineering scenarios, the larger the scene, the more challenging it becomes for the SfM method to perform reconstruction. This is a common issue with traditional SfM approaches, while the advantages of the proposed method become more pronounced.

From the above comparison, it is evident that our method enhances the LOAM approach by integrating image data. This upgrade enables semantic segmentation and reconstruction of cracks while maintaining the foundation of structural reconstruction. Furthermore, compared to the commonly used SfM method, the proposed approach achieves higher reconstruction quality,

faster reconstruction speed, and requires fewer data acquisition constraints. This makes it more suitable for practical engineering applications.

## 10 | CONCLUSIONS

By combining advanced computer vision techniques with multi-modal crack reconstruction, this study develops a novel system for robust and generalizable concrete crack segmentation, as well as precise, automated 3D crack reconstruction and measurement. The system is implemented on a handheld device equipped with a camera, LiDAR, and an IMU, integrated using multi-sensor fusion techniques. This design ensures compatibility with a wide variety of portable and mobile devices. Some specific conclusions can be made as follows:

1. This study initially innovatively proposed a highly generalizable crack segmentation method leveraging a segmentation base model, such as DeepLabv3+, which is further enhanced using the foundation model SAM. This approach enables the creation of precise 2D crack masks, even in complex and unfamiliar environments, effectively addressing challenges such as varying textures, lighting conditions, and noise.

2. To achieve high-precision 3D crack reconstruction, the study integrates LiDAR-generated point clouds with image data and segmentation masks. By employing a time-synchronized, multi-frame and multi-modal framework, the fusion of image and LiDAR-SLAM produces dense, colorized point clouds that accurately represent crack semantics at real-world scales. This approach enhances reconstruction accuracy and robustness, reliance on data quality during on-field acquisition, and simplifies operational complexity.
3. The study introduces an automatic, quantitative method for measuring the 3D geometric properties of cracks directly within the dense 3D point cloud space. This approach overcomes the limitations of traditional 2D measurements, providing accurate and adaptable method for assessing structural cracks across varying distances and complex geometries.
4. Finally, the proposed system is employed for the detection, reconstruction, and measurement of cracks on concrete structures under various conditions and with diverse shapes. Its effectiveness, accuracy, and robustness were validated through extensive comparisons with state-of-the-art methods, demonstrating the system's strong potential for real-world applications.

## ACKNOWLEDGMENT

This work was supported by the National Natural Science Foundation of China (project No. 2022HWYQ04, 52308225), the Natural Science Foundation of Hunan Province, China (project No. 2023JJ40721), Science and Technology Research and Development Program Project of China railway group limited (Major Special Project, No. 2021-Special-04-2), the Grant-in-Aid for Early-Career Scientists of Japan (20K14808), and the Kajima Foundation's International Joint Research Grant. Their support is gratefully acknowledged.

## REFERENCES

- Ahmadi, A., Khalesi, S. & Bagheri, M.A. (2018) Automatic road crack detection and classification using image processing techniques, machine learning and integrated models in urban areas: A novel image binarization technique. *Journal of Industrial and Systems Engineering*, 11, 85–97.
- Ahn, S.J., Yoo, J., Lee, B.G. & Lee, J.J. 3d surface reconstruction from scattered data using moving least square method. In: Roli, F. & Vitulano, S. (Eds.) *Image Analysis and Processing – ICIAP 2005, 2005*. Berlin, Heidelberg: Springer Berlin Heidelberg, pp. 719–726.
- Balta, H., Velagic, J., Bosschaerts, W., Cubber, G.D. & Siciliano, B. (2018) Fast statistical outlier removal based method for large 3 point clouds of outdoor environments. *IFAC-PapersOnLine*, 51(22), 348–353. doi:<https://doi.org/10.1016/j.ifacol.2018.11.566>.
- Bréhéret, A. (2017) *Pixel Annotation Tool*. <https://github.com/abreheret/PixelAnnotationTool>.
- Caron, M., Touvron, H., Misra, I., Jegou, H., Mairal, J., Bojanowski, P. et al. Emerging properties in self-supervised vision transformers. In: *2021 IEEE/CVF International Conference on Computer Vision (ICCV), 2021*. : IEEE, pp. 9630–9640.
- Cha, Y.J., Choi, W. & Büyüköktürk, O. (2017) Deep learning-based crack damage detection using convolutional neural networks. *Computer-Aided Civil and Infrastructure Engineering*, 32(5), 361–378. doi:[10.1111/mice.12263](https://doi.org/10.1111/mice.12263).
- Chaiyasarn, K., Khan, W., Ali, L., Sharma, M., Brackenbury, D. & Dejong, M. Crack detection in masonry structures using convolutional neural networks and support vector machines. In: Teizer, J. (Ed.) *Proceedings of the 35th International Symposium on Automation and Robotics in Construction (ISARC), Jul. 2018*. Taipei, Taiwan: International Association for Automation and Robotics in Construction (IAARC), pp. 118–125, iSSN: 2413-5844.
- Chen, L.C., Zhu, Y., Papandreou, G., Schroff, F. & Adam, H. Encoder-decoder with atrous separable convolution for semantic image segmentation. In: Ferrari, V., Hebert, M., Sminchisescu, C. & Weiss, Y. (Eds.) *Computer Vision – ECCV 2018, 2018*. Cham: Springer International Publishing, pp. 833–851.
- Chu, H. & Chun, P.j. (2024) Fine-grained crack segmentation for high-resolution images via a multiscale cascaded network. *Computer-Aided Civil and Infrastructure Engineering*, 39(4), 575–594. doi:<https://doi.org/10.1111/mice.13111>.
- Chun, P.j. & Kikuta, T. (2024) Self-training with bayesian neural networks and spatial priors for unsupervised domain adaptation in crack segmentation. *Computer-Aided Civil and Infrastructure Engineering*, 39(17), 2642–2661. doi:<https://doi.org/10.1111/mice.13315>.
- Dais, D., İhsan Engin Bal, Smyrou, E. & Sarhosis, V. (2021) Automatic crack classification and segmentation on masonry surfaces using convolutional neural networks and transfer learning. *Automation in Construction*, 125, 103606. doi:<https://doi.org/10.1016/j.autcon.2021.103606>.
- Deng, L., Sun, T., Yang, L. & Cao, R. (2023) Binocular video-based 3d reconstruction and length quantification of cracks in concrete structures. *Automation in Construction*, 148, 104743. doi:[10.1016/j.autcon.2023.104743](https://doi.org/10.1016/j.autcon.2023.104743).
- Deng, Z., Huang, M., Wan, N. & Zhang, J. (2023) The current development of structural health monitoring for bridges: A review. *Buildings*, 13(6). doi:[10.3390/buildings13061360](https://doi.org/10.3390/buildings13061360).
- Ding, W., Yang, H., Yu, K. & Shu, J. (2023) Crack detection and quantification for concrete structures using uav and transformer. *Automation in Construction*, 152, 104929. doi:[10.1016/j.autcon.2023.104929](https://doi.org/10.1016/j.autcon.2023.104929).
- Du, T., Zeng, Y.H., Yang, J., Tian, C.Z. & Bai, P.F. (2020) Multi-sensor fusion slam approach for the mobile robot with a bio-inspired polarised skylight sensor. *IET Radar, Sonar & Navigation*, 14(12), 1950–1957. doi:<https://doi.org/10.1049/iet-rsn.2020.0260>.
- Feng, C.Q., Li, B.L., Liu, Y.F., Zhang, F., Yue, Y. & Fan, J.S. (2023) Crack assessment using multi-sensor fusion simultaneous localization and mapping (slam) and image super-resolution for bridge inspection. *Automation in Construction*, 155, 105047. doi:<https://doi.org/10.1016/j.autcon.2023.105047>.
- Flah, M., Suleiman, A.R. & Nehdi, M.L. (2020) Classification and quantification of cracks in concrete structures using deep learning image-based techniques. *Cement and Concrete Composites*, 114, 103781. doi:[10.1016/j.cemconcomp.2020.103781](https://doi.org/10.1016/j.cemconcomp.2020.103781).
- Furgale, P., Barfoot, T.D. & Sibley, G. Continuous-time batch estimation using temporal basis functions. In: *2012 IEEE International Conference on Robotics and Automation, 2012*, pp. 2088–2095.
- Furgale, P., Rehder, J. & Siegwart, R. Unified temporal and spatial calibration for multi-sensor systems. In: *2013 IEEE/RSJ International Conference on Intelligent Robots and Systems, 2013*, pp. 1280–1286.
- Hao, H., Bi, K., Chen, W., Pham, T.M. & Li, J. (2023) Towards next generation design of sustainable, durable, multi-hazard resistant, resilient, and smart civil engineering structures. *Engineering Structures*, 277, 115477. doi:<https://doi.org/10.1016/j.engstruct.2022.115477>.
- Hu, K., Chen, Z., Kang, H. & Tang, Y. (2024) 3d vision technologies for a self-developed structural external crack damage recognition robot. *Automation in Construction*, 159, 105262. doi:<https://doi.org/10.1016/j.autcon.2023.105262>.
- Huang, Y., Liu, Y., Liu, F. & Liu, W. (2024) A lightweight feature attention fusion network for pavement crack segmentation. *Computer-Aided Civil and Infrastructure Engineering*, 39(18), 2811–2825. doi:<https://doi.org/10.1111/mice.13225>.
- Iglovikov, V. & Shvets, A. (2018) Ternaunet: U-net with vgg11 encoder pre-trained on imagenet for image segmentation. *ArXiv e-prints*.
- Junior, G.S., Ferreira, J., Millán-Arias, C., Daniel, R., Junior, A.C. & Fernandes, B.J.T. (2021) Ceramic cracks segmentation with deep learning. *Applied Sciences*, 11(13). doi:[10.3390/app1136017](https://doi.org/10.3390/app1136017).
- Katz, S., Tal, A. & Basri, R. (2007) Direct visibility of point sets. In: *ACM SIGGRAPH 2007 papers*pp. 24–es.



- Ke, L., Ye, M., Danelljan, M., Tai, Y.W., Tang, C.K., Yu, F. et al. (2024) Segment anything in high quality. *Advances in Neural Information Processing Systems*, 36.
- Kim, B. & Cho, S. (2019) Image-based concrete crack assessment using mask and region-based convolutional neural network. *Structural Control and Health Monitoring*, 26(8), e2381. doi:10.1002/stc.2381.
- Kim, H., Sim, S.H. & Spencer, B.F. (2022) Automated concrete crack evaluation using stereo vision with two different focal lengths. *Automation in Construction*, 135, 104136. doi:10.1016/j.autcon.2022.104136.
- Kirillov, A., Mintun, E., Ravi, N., Mao, H., Rolland, C., Gustafson, L. et al. Segment anything. In: *Proceedings of the IEEE/CVF International Conference on Computer Vision, 2023*, pp. 4015–4026.
- Koide, K., Oishi, S., Yokozuka, M. & Banno, A. General, single-shot, target-less, and automatic lidar-camera extrinsic calibration toolbox. In: *2023 IEEE International Conference on Robotics and Automation (ICRA). IEEE, 2023*, pp. 11301–11307.
- Li, Y., Gu, C., Dullien, T., Vinyals, O. & Kohli, P. (2019) *Graph matching networks for learning the similarity of graph structured objects*.
- Lin, J. & Zhang, F. R3live: A robust, real-time, rgb-colored, lidar-inertial-visual tightly-coupled state estimation and mapping package. In: *2022 International Conference on Robotics and Automation (ICRA), 2022*, pp. 10672–10678.
- Liu, H., Li, C., Wu, Q. & Lee, Y.J. (2023) *Visual instruction tuning*.
- Liu, Y., Fan, J., Nie, J., Kong, S. & Qi, Y. (2021) A review and prospect of digital image method for crack identification on structural surfaces. *Journal of Civil Engineering*, 54(06), 79–98. doi:10.15951/j.tmgxcb.2021.06.008.
- Liu, Y., Yao, J., Lu, X., Xie, R. & Li, L. (2019) Deepcrack: A deep hierarchical feature learning architecture for crack segmentation. *Neurocomputing*, 338, 139–153. Publisher: Elsevier.
- Liu, Y., Zhang, W. & Wang, J. Source-free domain adaptation for semantic segmentation. In: *Proceedings of the IEEE/CVF Conference on Computer Vision and Pattern Recognition, 2021b*, pp. 1215–1224.
- Liu, Z., Lin, Y., Cao, Y., Hu, H., Wei, Y., Zhang, Z. et al. Swin transformer: Hierarchical vision transformer using shifted windows. In: *Proceedings of the IEEE/CVF International Conference on Computer Vision (ICCV), 2021c*.
- Lu, H., You, K., Feng, W., Zhou, N., Fridley, D., Price, L. et al. (2024) Reducing china's building material embodied emissions: Opportunities and challenges to achieve carbon neutrality in building materials. *iScience*, 27(3), 109028. doi:https://doi.org/10.1016/j.isci.2024.109028.
- Mirzazade, A., Popescu, C., Gonzalez-Libreros, J., Blanksvärd, T., Täljsten, B. & Sas, G. (2023) Semi-autonomous inspection for concrete structures using digital models and a hybrid approach based on deep learning and photogrammetry. *Journal of Civil Structural Health Monitoring*, 13(8), 1633–1652. doi:10.1007/s13349-023-00680-x.
- Nelder, J.A. & Mead, R. (1965) A simplex method for function minimization. *The Computer Journal*, 7(4), 308–313. doi:10.1093/comjnl/7.4.308.
- OpenAI, Achiam, J., Adler, S., Agarwal, S., Ahmad, L., Akkaya, I. et al. (2024) *Gpt-4 technical report*.
- Pak, M. & Kim, S. Crack detection using fully convolutional network in wall-climbing robot. In: Park, J.J., Fong, S.J., Pan, Y. & Sung, Y. (Eds.) *Advances in Computer Science and Ubiquitous Computing, 2021*. Singapore: Springer Singapore, pp. 267–272.
- Pantoja-Rosero, B.G., Oner, D., Kozinski, M., Achanta, R., Fua, P., Perez-Cruz, F. et al. (2022) Topo-loss for continuity-preserving crack detection using deep learning. *Construction and Building Materials*, 344, 128264. doi:10.1016/j.conbuildmat.2022.128264.
- Pennec, X. (1998) Computing the mean of geometric features application to the mean rotation. Ph.D. thesis, INRIA.
- Radford, A., Kim, J.W., Hallacy, C., Ramesh, A., Goh, G., Agarwal, S. et al. Learning transferable visual models from natural language supervision. In: *Proceedings of the 38th International Conference on Machine Learning, 2021*. : PMLR, pp. 8748–8763, ISSN: 2640-3498.
- Sarlin, P.E., DeTone, D., Malisiewicz, T. & Rabinovich, A. Superglue: Learning feature matching with graph neural networks. In: *Proceedings of the IEEE/CVF Conference on Computer Vision and Pattern Recognition (CVPR), June 2020*.
- Shokri, P., Shahbazi, M. & Nielsen, J. (2022) Semantic segmentation and 3d reconstruction of concrete cracks. *Remote Sensing*, 14(22), 5793. doi:10.3390/rs14225793.
- Silva, W.R.L.d. & Lucena, D.S.d. (2018) Concrete cracks detection based on deep learning image classification. *Proceedings*, 2(8), 489. doi:10.3390/ICEM18-05387, number: 8 Publisher: Multidisciplinary Digital Publishing Institute.
- Stewart, A.D. & Newman, P. Laps - localisation using appearance of prior structure: 6-dof monocular camera localisation using prior pointclouds. In: *2012 IEEE International Conference on Robotics and Automation, 2012*, pp. 2625–2632.
- Sun, L., Shang, Z., Xia, Y., Bhowmick, S. & Nagarajiah, S. (2020) Review of bridge structural health monitoring aided by big data and artificial intelligence: From condition assessment to damage detection. *Journal of Structural Engineering*, 146(5), 04020073. doi:10.1061/(ASCE)ST.1943-541X.0002535.
- Sun, L., Yang, Y., Zhou, G., Chen, A., Zhang, Y., Cai, W. et al. (2024) An integration–competition network for bridge crack segmentation under complex scenes. *Computer-Aided Civil and Infrastructure Engineering*, 39(4), 617–634. doi:https://doi.org/10.1111/mice.13113.
- Tang, W., Huang, S., Zhao, Q., Li, R. & Huangfu, L. (2022) An iteratively optimized patch label inference network for automatic pavement distress detection. *IEEE Transactions on Intelligent Transportation Systems*, 23(7), 8652–8661. doi:10.1109/TITS.2021.3084809.
- Touvron, H., Martin, L., Stone, K., Albert, P., Almahairi, A., Babaei, Y. et al. (2023) *Llama 2: Open foundation and fine-tuned chat models*.
- Wang, K., Liew, J.H., Zou, Y., Zhou, D. & Feng, J. Panet: Few-shot image semantic segmentation with prototype alignment. In: *proceedings of the IEEE/CVF international conference on computer vision, 2019*, pp. 9197–9206.
- Xu, S., Yuan, H., Shi, Q., Qi, L., Wang, J., Yang, Y. et al. (2024) Rap-sam: Towards real-time all-purpose segment anything. *arXiv preprint arXiv:2401.10228*,.
- Xu, W., Cai, Y., He, D., Lin, J. & Zhang, F. (2022) Fast-lio2: Fast direct lidar-inertial odometry. *IEEE Transactions on Robotics*, 38(4), 2053–2073. doi:10.1109/TRO.2022.3141876.
- Xu, W. & Zhang, F. (2021) Fast-lio: A fast, robust lidar-inertial odometry package by tightly-coupled iterated kalman filter. *IEEE Robotics and Automation Letters*, 6(2), 3317–3324. doi:10.1109/LRA.2021.3064227.
- Yang, L., Li, B., Feng, J., Yang, G., Chang, Y., Jiang, B. et al. (2023) Automated wall-climbing robot for concrete construction inspection. *Journal of Field Robotics*, 40(1), 110–129. doi:10.1002/rob.22119.
- Yang, L., Li, B., Li, W., Jiang, B. & Xiao, J. Semantic metric 3d reconstruction for concrete inspection. In: *2018 IEEE/CVF Conference on Computer Vision and Pattern Recognition Workshops (CVPRW), Jun. 2018a*. Salt Lake City, UT, USA: IEEE, pp. 1624–16248.
- Yang, X., Li, H., Yu, Y., Luo, X., Huang, T. & Yang, X. (2018) Automatic pixel-level crack detection and measurement using fully convolutional network. *Computer-Aided Civil and Infrastructure Engineering*, 33(12), 1090–1109. doi:10.1111/mice.12412.
- Yao, Y., Tung, S.T.E. & Glisic, B. (2014) Crack detection and characterization techniques—an overview. *Structural Control and Health Monitoring*, 21(12), 1387–1413.
- Zeng, Q., Fan, G., Wang, D., Tao, W. & Liu, A. (2024) A systematic approach to pixel-level crack detection and localization with a feature fusion attention network and 3d reconstruction. *Engineering Structures*, 300, 117219. doi:10.1016/j.engstruct.2023.117219.
- Zhang, J. & Singh, S. Loam: Lidar odometry and mapping in real-time. In: *Robotics: Science and Systems. Vol. 2, 2014*.
- Zhang, L., Yang, F., Daniel Zhang, Y. & Zhu, Y.J. Road crack detection using deep convolutional neural network. In: *2016 IEEE International Conference on Image Processing (ICIP), Sep. 2016*, pp. 3708–3712, iSSN: 2381-8549.
- Zhang, Z., Shen, Z., Liu, J., Shu, J. & Zhang, H. (2023) A binocular vision-based crack detection and measurement method incorporating semantic segmentation. *Sensors*, 24(1), 3. doi:10.3390/s24010003.

- Zhao, S., Kang, F. & Li, J. (2024) Intelligent segmentation method for blurred cracks and 3d mapping of width nephograms in concrete dams using uav photogrammetry. *Automation in Construction*, 157, 105145. doi:10.1016/j.autcon.2023.105145.
- Zhou, Z., Zhang, J. & Gong, C. (2022) Automatic detection method of tunnel lining multi-defects via an enhanced you only look once network. *Computer-Aided Civil and Infrastructure Engineering*, 37(6), 762–780. doi:https://doi.org/10.1111/mice.12836.
- Zhou, Z., Zhang, J. & Gong, C. (2023) Hybrid semantic segmentation for tunnel lining cracks based on swin transformer and convolutional neural network. *Computer-Aided Civil and Infrastructure Engineering*, 38(17), 2491–2510. doi:https://doi.org/10.1111/mice.13003.
- Zou, Q., Cao, Y., Li, Q., Mao, Q. & Wang, S. (2012) Cracktree: Automatic crack detection from pavement images. *Pattern Recognition Letters*, 33(3), 227–238. doi:10.1016/j.patrec.2011.11.004.
- Zou, Y., Yu, Z., Kumar, B. & Wang, J. Unsupervised domain adaptation for semantic segmentation via class-balanced self-training. In: *Proceedings of the European conference on computer vision (ECCV), 2018*, pp. 289–305.